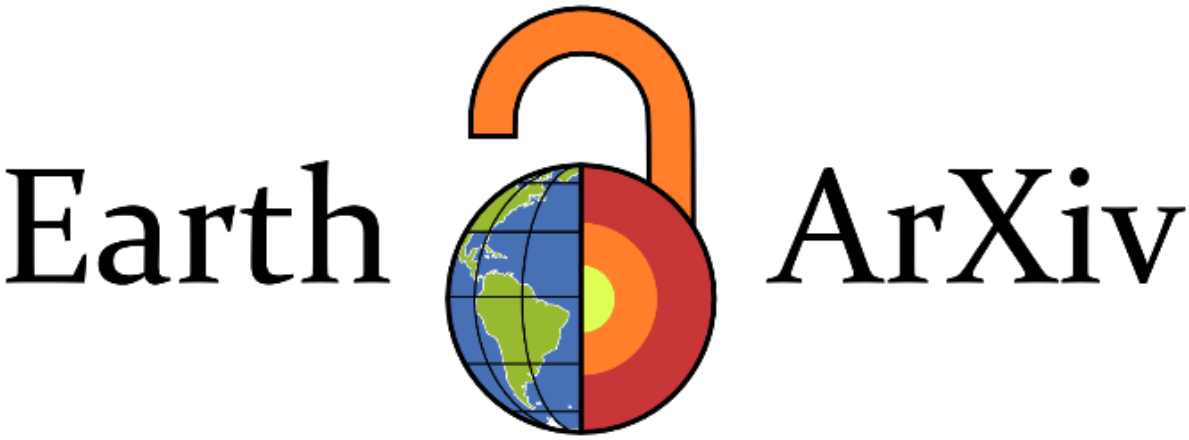

Q_{M1D}: A 1D model of shear attenuation in the mantle from differential body waves

Carl Martin[1,2*], Sujania Talavera-Soza[1] & Arwen Deuss[1]

[1] Department of Geosciences, Utrecht University, 3584 CB, Netherlands

[2] Research School of Earth Sciences, The Australian National University, Canberra, ACT 0200, Australia

*Corresponding author (carl.martin@anu.edu.au)

Abstract

We introduce a new 1D model of shear attenuation in the mantle (Q_{M1D}) constructed from measurements of differential attenuation of S and ScS. We build a data set of over 94,000 measurements of $\delta t^*_{\mathrm{ScS\text{-}S}}$ from seismograms with high quality S and ScS waveforms from deep earthquakes between 20–75° epicentral distance from 1990–2024. To ensure that measurements are robust, we require that values of differential attenuation are similar between the instantaneous frequency matching and waveform matching methods. Using this data set, we perform a Bayesian inversion to construct 1D profiles of mantle shear attenuation Q_μ and its uncertainties. Our data set has a high sensitivity to the mid-mantle (750–2200 km) corresponding to the turning depths of the S phases, which maps into lower uncertainty in the ensemble distribution at these depths. Q_{M1D} suggests that the mantle is more highly attenuating than PREM on average; but, notably, that there are low attenuating layers around 900 km and 2000 km depth. Due to the source-receiver distribution for the phases, there is a sampling bias in the mantle around the edge of the Pacific. These weakly attenuating zones in the mantle may correspond to regions of slab stagnation around 900 km and potentially a viscosity jump in the deep mantle around 2000 km depth.

1 Introduction

Over the past decades, elastic tomography models of the mantle have been numerous and are becoming increasingly detailed [e.g. Dziewonski and Anderson, 1984; Ritsema et al., 2011; Cui et al., 2024]. However, it is equally important to understand the anelastic structure since it results in variations in the amplitude of seismic phases [e.g. Romanowicz, 1995; Dalton and Ekström, 2006; Zaroli et al., 2010; Hansen et al., 2021] – which may otherwise be mapped into elastic structure [e.g. Karato, 1993; Chaves and Ritsema, 2016] – but also because the anelastic structure is thought to be much more sensitive to temperature and grain size variations in the mantle than elastic structure is [e.g. Jackson et al., 1992, 2002; Matas and Bukowinski, 2007; Faul and Jackson, 2015]. Knowledge of both elastic and anelastic structure will therefore result in important additional constraints on mantle dynamics, but also in distinguishing between the chemical and thermal composition of the mantle [e.g. Romanowicz, 1995; Cooper, 2002; Gung and Romanowicz, 2004].

Whilst the anelastic structure of upper mantle, i.e. attenuation, is relatively well understood from body and surface waves [e.g. Romanowicz, 1995; Bhattacharyya et al., 1996; Reid et al., 2001; Gung and Romanowicz, 2004; Dalton et al., 2008; Karaoğlu and Romanowicz, 2018; Adenis et al., 2017] – where a large scale anti-correlation is found between velocity and attenuation – there have been significantly fewer studies on attenuation in the lower mantle. The low degree attenuation structure of the lower mantle is predominantly constrained by normal mode observations [e.g. Dziewonski and Anderson, 1984; Moulik and Ekström, 2025] and is typically assumed to be less attenuating than the upper mantle [e.g. Warren and Shearer, 2002; Souriau et al., 2012; Nguyen et al., 2025]. There have been attempts to distinguish relative attenuation within and outside the two antipodal large low velocity provinces (LLVPs) using body [Romanowicz, 1995; Hwang and Ritsema, 2011; Liu and Grand, 2018] to provide much needed constraints on the grain size, temperature, and longevity of these structures. A recent study by Talavera-Soza et al. [2025] used anelastic normal mode splitting functions observations to construct a 3D model of attenuation of the mantle. Their model, QS4L3, is in good agreement with attenuation observations from body waves and surface waves in the upper mantle [e.g. Bhattacharyya et al., 1996; Reid et al., 2001; Romanowicz and Gung, 2002; Dalton et al., 2008; Karaoğlu and Romanowicz, 2018; Adenis et al., 2017], but appears to differ from the few studies of the lowermost mantle which use body

waves. In particular, normal modes find LLVPs to be weakly attenuating – suggesting large grain sizes and high temperatures, and potentially implies a long-lived structure [Talavera-Soza et al., 2025] – whilst body waves studies have suggested the opposite [Romanowicz, 1998; Lawrence and Wysession, 2006; Hwang and Ritsema, 2011; Liu and Grand, 2018]. It is important to note that the datasets used in each of the studies of the lower mantle are small and that the frequency content differs by a few orders of magnitude between body waves and normal modes. Given there is significant variability and scatter in measurements of attenuation [e.g. Bhattacharyya, 1998], the nature of anelasticity in the lowermost mantle remains unclear. In this study, we therefore aim to elucidate the anelastic structure of the lower mantle.

Attenuation t^* (with units of seconds) of a body wave phase is defined as the shear quality factor Q_μ (dimensionless) integrated along the raypath

$$t^* = \int \frac{\mathrm{d}s}{\beta\, Q_\mu} = \int_s \frac{\mathrm{d}t}{Q_\mu} \tag{1}$$

where s defines the raypath and β is the shear velocity. This is also sometimes related to the path averaged quality factor Q_{phase} as $t^* = T_{\text{phase}}/Q_{\text{phase}}$ for the total travel time T_{phase} of a given body wave phase. It is not possible to directly measure t^*, but it is possible to measure the relative attenuation between a target phase with t^*_{TARG} and a reference phase with t^*_{REF} as

$$\delta t^*_{\text{REF-TARG}} = t^*_{\text{REF}} - t^*_{\text{TARG}} = \int_{\text{REF}} \frac{\mathrm{d}t}{Q_\mu} - \int_{\text{TARG}} \frac{\mathrm{d}t}{Q_\mu} \tag{2}$$

There have been many methods used over the past decades to make measurements of relative attenuation of body waves. These can be categorised as frequency domain or time domain methods, but the principle of both methods is the same: when a signal is attenuated, the higher frequency content is more attenuated than the lower frequency content [e.g. Teng, 1968; Quan and Harris, 1997]. In the frequency domain, the spectral ratio (SR) method is by far the most commonly used method [e.g. Sheehan and Solomon, 1992; Bhattacharyya et al., 1996; Roth et al., 1999; Fisher et al., 2003; Lawrence and Wysession, 2006; Hwang and Ritsema, 2011; Suetsugu et al., 2019; Soto Castaneda et al., 2021; Nguyen et al., 2025], which relates the spectral amplitude ratio to the relative attenuation between two signals. A more sophisticated frequency domain method – the

instantaneous frequency matching method (IFM) – applies the causal attenuation operator to the target signal until its instantaneous frequency matches that of the reference signal [e.g. Matheney and Nowack, 1995; Quan and Harris, 1997; Ford et al., 2012; Durand et al., 2013; Sun et al., 2025]. In the time domain, the waveform matching (WM) method finds the optimal relative attenuation that matches the waveforms between the target signal which has been attenuated by the causal attenuation operator and the reference signal [e.g. Chan and Der, 1988; Bhattacharyya, 1998; Reid et al., 2001; Oki and Shearer, 2008; Bezada et al., 2023]. This is also sometimes done in a joint inversion for the amplitude ratio, time delay and source parameters [e.g. Reid et al., 2001; Garcia et al., 2013; Pejić et al., 2017]. Additionally, implicit inversion of Q_μ structure has also been performed by waveform modelling of amplitude ratios [e.g. Revenaugh and Jordan, 1991; Konishi et al., 2017, 2020; Borgeaud and Deschamps, 2021], but this has significant trade-offs with elastic structure. Each of these methods has its own advantages and disadvantages – and no one method works in every situation [e.g. Bhattacharyya, 1998; Ford et al., 2012] – so the most appropriate method(s) to use depends on the context of the investigation. It is important to note that all of the methods described above result in inaccurate estimates of attenuation when there are interfering phases in the target or reference seismic waveforms.

The choice of which reference and target signals to use can also be broadly categorised into three different types:

1. The first is to estimate the relative attenuation of the target and reference signals for two different seismic phases recorded on the same station for the same event; e.g. ScSScS-ScS [Revenaugh and Jordan, 1991], sS-S and sScS-ScS [Flanagan and Wiens, 1994], and ScS-S [Durand et al., 2013]. Any differential attenuation is then attributed to the difference between the two raypaths travelled by the two phases, since the source and receiver contributions to attenuation are very similar for both raypaths.

2. The second is to estimate the attenuation of the same seismic phase for the same event recorded on different stations. In this case, the source term – the contribution to the measurement as a result of source effects – is negligible since the paths travelled by a phase are similar near the source, but a station term – the contribution to the measurement as a result of near-station effects – must be accounted for. However, one important consideration in us-

ing this method is that rupture directivity modifies the source frequency spectra as a function of the take-off angle [e.g. Bernard et al., 1996], so any inferred attenuation difference between pairwise stations includes both differential attenuation structure and source frequency spectra variations [e.g. Warren and Shearer, 2006]. To overcome this, station pairs can be chosen so that they are azimuthally similar [e.g. Hwang and Ritsema, 2011].

3. The third is to estimate the 'absolute' attenuation of an observed phase relative to synthetic waveforms, in which case both source and station effects must be accounted for in the synthetic modelling in order to get accurate results [e.g. Zhu et al., 2022; Sun et al., 2025]. Equivalently, by assuming a source model and the station response [e.g. Brune, 1970; Scherbaum, 1990], it is possible to estimate the 'absolute' attenuation of a signal by directly fitting its frequency spectra [e.g. Rietbrock, 2001; Eberhart-Phillips and Chadwick, 2002].

Source and station terms can be inverted for – as well as Q_μ, but at additional computational expense – assuming that these terms are consistent for a given source or station, and that individual sources and stations are represented in the dataset multiple times [e.g. Roth et al., 1999; Warren and Shearer, 2002; Hwang et al., 2009]. Historically, ScS reverberations have been used to make whole mantle average estimates of Q_{ScS} in corridors between sources and receivers [e.g. Chan and Der, 1988; Revenaugh and Jordan, 1991; Isse and Nakanishi, 1997; Gomer and Okal, 2003; Kanamori and Rivera, 2015; Chaves and Ritsema, 2016], which minimises the effect of source and station terms. However, this choice of phases involves unpaired raypaths travelling through the upper mantle and crust, so accurate upper mantle and crustal models are required to correct for these effects or the results could be significantly biased [e.g. Revenaugh and Jordan, 1991; Isse and Nakanishi, 1997]. This is also the case when comparing synthetics to data to estimate attenuation [e.g. Sun et al., 2025].

Ford et al. [2012] and Durand et al. [2013] used S and ScS – which minimises the effects of source and station terms, and has no unpaired raypaths travelling through the crust – to estimate the shear attenuation profile of the mantle. S turns in the mid-mantle, whilst ScS is reflected off the CMB (Figure 1a). At long epicentral distances, the raypaths of S and ScS, and the take-off and incident angles, are very similar (Figures 1a & S1c), but the travel time differential becomes too small to distinguish between them on seismograms (Figure 1b). At short epicentral distances, the

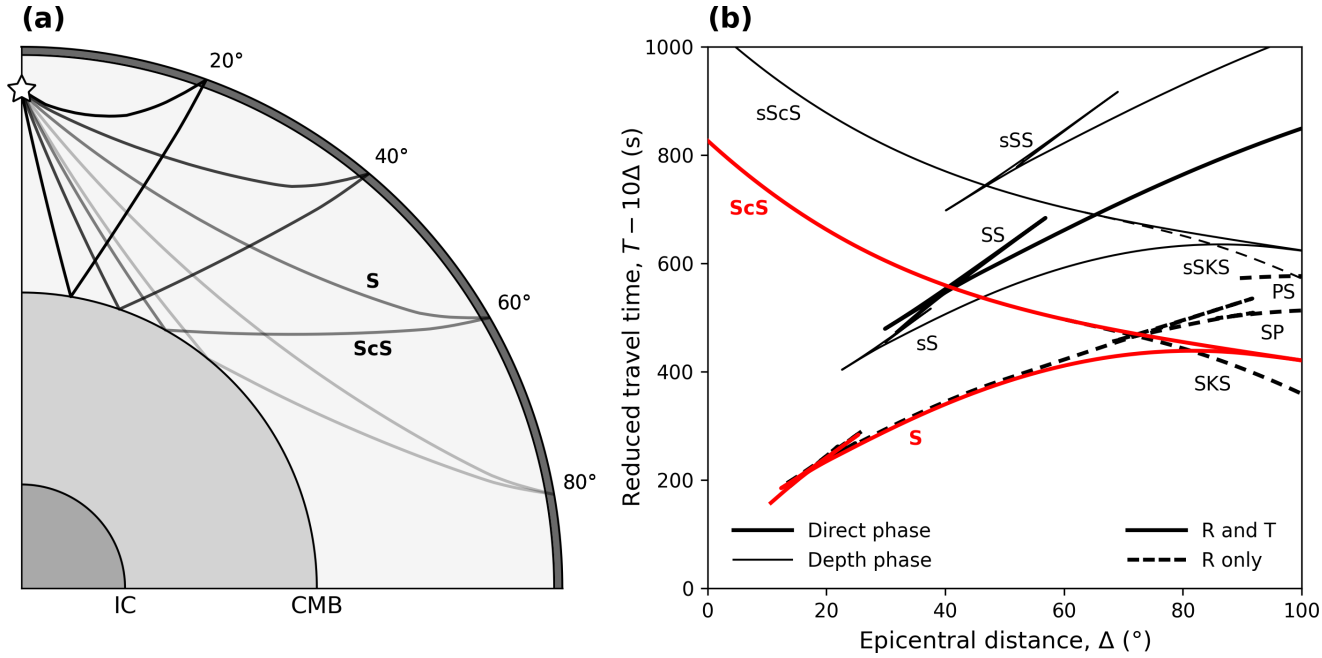

Figure 1: **(a)** S and ScS raypaths for a range of epicentral distances. The turning depths of S and differential incident and take-off angles of S and ScS are shown in Figure S1. **(b)** The reduced travel times of seismic phases observed around S and ScS (highlighted in red). The visibility of phases on different components for an isotropic model is indicated as R and T or R only.

difference in take-off and incident angles becomes large, and so the assumption that the near-source terms cancel out becomes strained [e.g. Ford et al., 2012]. However, some have suggested that this effect is negligible for frequency domain methods, even for phases with opposite take-off angles [e.g. Flanagan and Wiens, 1994]. The differential attenuation of ScS and S is sensitive to the whole depth range of the mantle, but significantly less sensitive in the upper mantle where the raypaths are most similar. Assuming a radially isotropic Earth, the relative attenuation of ScS and S would predominantly depend on the turning depth of the S raypath (Figures 1a & S1a-b).

In this study, we compile a dataset of 100,000 high quality S and ScS waveforms and estimate the relative attenuation $\delta t^*_{\text{ScS-S}}$ to make inferences about mantle shear attenuation. We evaluate three commonly used methods to estimate differential attenuation (SR, IFM and WM). After weighing the advantages and disadvantages of each of the methods, we disregard the spectral ratio method (SR), and analyse and compare our dataset of S and ScS waveforms with the instantaneous frequency matching (IFM) and waveform matching (WM) methods. Finally, we perform a Bayesian inversion to fit a 1D whole mantle model of Q_μ to our dataset, which also includes estimates of uncertainty in the profile.

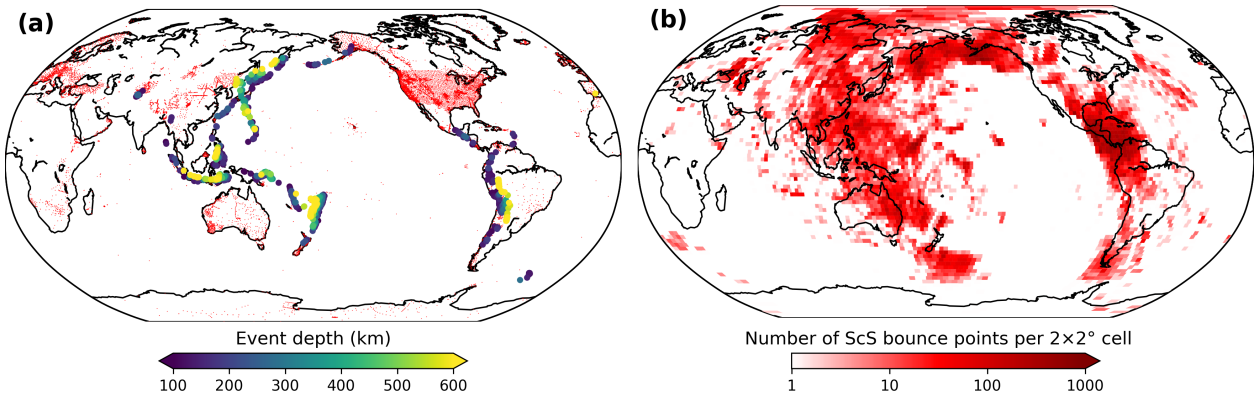

Figure 2: **(a)** Locations of earthquakes (circles, coloured by event depth) and stations (red dots) used in this study. **(b)** Number of ScS bounce points per $2 \times 2°$ quasi-equal area cell.

2 Methods

2.1 Data

We inspected seismograms of earthquakes larger than magnitude 6.0 and deeper than 75 km depth between 1990–2024 from the NSF SAGE event catalogue. We only downloaded seismograms for stations between epicentral distances 20–80°, since S is not distinguishable from surface waves at shorter distances and ScS at longer distances. We ensure that S phases at short epicentral distances do not appear to be contaminated by triplication, which may result in phase broadening. 75 km is chosen as the depth threshold since the arrival time difference between S and ScS and their respective depth phases (sS and sScS) is twice the dominant period of S (∼14 s). The instrument response is removed and output as velocity, before being downsampled to 10 Hz and rotated to the ZRT orientation.

To avoid issues of seismic phase interference in our measurements, we disregard seismograms for which the arrival time of ScS is within 25 s of S, sS, SS or SSS – approximately twice the dominant period of S waves – as predicted by PREM [Preliminary Reference Earth Model; Dziewonski and Anderson, 1984]. We then compute the signal-to-noise (SNR) of the seismic phases, defined as the ratio between the maximum amplitude ±15 s around the predicted S or ScS arrival and the root mean square of the window 120–20 s before the predicted S arrival. We then discard any seismograms for which the SNR of S or ScS are less than 5, or if the maximum amplitude in the 30 s window around the phase is at the edge of the window.

The sources and receivers represented in our final dataset are shown in Figure 2a. For a quasi-equal area grid of the core-mantle boundary (CMB), we plot the number of ScS bounce points per $2 \times 2^{\circ}$ cell in Figure 2b, which shows that our dataset is strongly biased towards the source-receiver coverage around the edge of the Pacific.

2.2 Estimating differential attenuation of body waves

2.2.1 Spectral ratio method

The spectral ratio (SR) method of estimating relative attenuation has been known for over 60 years [e.g. Asada and Takano, 1963; Kovach and Anderson, 1964], in which the gradient of the spectral ratio between two signals can be related to the relative attenuation between the signals assuming frequency-independence of Q. This method suffers from significant technical challenges pertaining to the windowing and tapering of signals, spectral gaps, and the choice of frequency range over which to estimate the gradient of the spectral ratio [e.g. Bhattacharyya, 1998; Ford et al., 2012]. Whilst these shortfalls have been resolved to some extent – e.g. using multi-tapering of seismic phases to reduce spectral leakage [Thomson, 1982; Lees and Park, 1995] – we find that the calculated δt^* values depend strongly on the setup parameters and signal-to-noise ratio (SNR) of the data. Notably, there was often very low similarity between the spectral ratio and its best linear fit, as previously observed by Isse and Nakanishi [1997]. To improve the quality of fit, some studies have also stacked data within a vertical column from ScS multiples and surface reflections to increase the SNR of the stacked data [e.g. Gomer and Okal, 2003; Suetsugu et al., 2019] – though this assumption is only reasonable for short epicentral distances and not practical for a broader global study – or performed joint fitting of spectral phase and amplitude ratios [e.g. Eilon and Abers, 2017].

2.2.2 Instantaneous frequency matching method

As attenuation preferentially diminishes higher frequency spectra, the average and peak frequencies will appear lower for more attenuated waves [e.g. Matheney and Nowack, 1995; Quan and Harris, 1997]. Matheney and Nowack [1995] derived that the differential attenuation between two signals is equivalent to the value of the causal attenuation operator t^*_{CAO} that matches the instantaneous

frequency of the target signal f^*_{TARG} to that of the reference signal f_{REF} (Figure 3a-e). The causal attenuation operator $D(\omega)$ takes the form

$$D(\omega) = \exp\left[\frac{-\omega t^*_{\mathrm{CAO}}}{2}\left(1 - \frac{2i}{\pi}\ln\frac{\omega}{\omega_0}\right)\right] \tag{3}$$

where t^*_{CAO} is the relative attenuation factor between two phases, ω is angular frequency, and ω_0 is a reference angular frequency (usually taken to be 1 Hz) [e.g. Chapman et al., 1988; Aki and Richards, 2002]. Since $t^*_{\mathrm{CAO}} \geq 0$ s, whichever signal has the lowest instantaneous frequency is the reference and the other is the target signal (Figure 3c-e).

The instantaneous amplitude (envelope) $a(t)$ and instantaneous phase $\phi(t)$ of a signal $y(t)$ represented as a complex function are given as

$$y(t) = a(t)\exp\left[i\phi(t)\right], \qquad a(t) = \sqrt{y(t)^2 + y^*(t)^2}, \qquad \phi(t) = \tan^{-1}\left[\frac{y^*(t)}{y(t)}\right] \tag{4}$$

where $y^*(t)$ is the Hilbert transform of a signal $y(t)$, so the instantaneous frequency is given by

$$f_{\mathrm{I}}(t) = \frac{1}{2\pi}\frac{\mathrm{d}\phi(t)}{\mathrm{d}t} = \frac{1}{2\pi}\frac{y(t)\frac{\mathrm{d}y^*(t)}{\mathrm{d}t} - y^*(t)\frac{\mathrm{d}y(t)}{\mathrm{d}t}}{a^2(t) + \epsilon^2} \tag{5}$$

where ϵ is a small damping factor.

It can be shown that the instantaneous centre frequency of the signal can be related to the instantaneous frequency

$$f_{\mathrm{C}} = \frac{\int_0^\infty f A(f)\,\mathrm{d}f}{\int_0^\infty A(f)\,\mathrm{d}f} \equiv \frac{\int_0^\infty f_{\mathrm{I}}(t)a(t)^2\,\mathrm{d}t}{\int_0^\infty a(t)^2\,\mathrm{d}t} \tag{6}$$

where $A(f)$ is the Fourier power spectrum [e.g. Barnes, 1993; Dasios et al., 2001], so the time-averaged instantaneous centre frequency is

$$f_{\mathrm{C}}(t) \approx \frac{\int_{t-W}^{t+W} f_{\mathrm{I}}(t')a(t')^2\,\mathrm{d}t'}{\int_{t-W}^{t+W} a(t')^2\,\mathrm{d}t'} \tag{7}$$

for a window of length $2W$ [Matheney and Nowack, 1995].

We perform an iterative search across t^*_{CAO} values with $W = 5$ s, beginning from 0–10 s in increments of 1 s and decreasing by factors of 10 until we reach a precision of 10^{-2} s. For S and

ScS, if $f_S < f_{ScS}$ (i.e. S is more attenuated than ScS) then S is the reference phase and ScS is the target phase, so $\delta t^*_{\text{ScS-S}} = -t^*_{\text{CAO}}$; otherwise $\delta t^*_{\text{ScS-S}} = t^*_{\text{CAO}}$ [e.g. Ford et al., 2012; Durand et al., 2013].

2.2.3 Waveform matching method

Time domain methods have also been used to estimate relative attenuation of seismic phases [e.g. Bhattacharyya, 1998; Reid et al., 2001]. The amplitude spectrum of S and ScS can be written as

$$A_S(\omega, \theta, \Delta) = S(\omega)\ R(\omega)\ I(\omega)\ G_S(\Delta)\ D(\omega, t^*_S)\ \exp[-i\omega t_S] \tag{8}$$

$$A_{ScS}(\omega, \theta, \Delta) = S(\omega)\ R(\omega)\ I(\omega)\ G_{ScS}(\Delta)\ D(\omega, t^*_{ScS})\ \exp[-i\omega t_{ScS}] \tag{9}$$

where ω is the angular frequency, θ is the take-off angle, Δ is the epicentral distance, $S(\omega)$ is the source spectrum, $R(\omega)$ is the site response, $I(\omega)$ is the instrument response, $G(\omega, \Delta)$ includes the source radiation pattern and geometric spreading, $D(\omega)$ is the causal attenuation operator as defined in Equation 3, and t_S and t_{ScS} are the travel times of S and ScS, respectively [e.g. Reid et al., 2001]. Assuming that the source spectrum, site response and instrument response are similar for both phases, we can relate the spectra of S and ScS as

$$A_{ScS}(\omega, \theta, \Delta) = G_{\text{ScS-S}}(\Delta)\ A_S(\omega, \theta, \Delta)\ D(\omega, \delta t^*_{\text{ScS-S}})\ \exp[-i\omega \delta t_{\text{ScS-S}}] \tag{10}$$

where $G_{\text{ScS-S}}(\Delta) = G_{ScS}(\Delta)/G_S(\Delta)$ is a constant, $\delta t^*_{\text{ScS-S}} = t^*_{ScS} - t^*_S$ and $\delta t_{\text{ScS-S}} = t_{ScS} - t_S$. For S and ScS, the assumption that the source spectra of both signals is the same is reasonable, as long as the take-off angles of the two phases are in the same lobe of the radiation pattern [e.g. Flanagan and Wiens, 1994].

In the time domain, the relative attenuation operator can therefore be found simply by minimising the misfit between the reference and attenuated target waveforms (Figure 3f-g), which we quantify using the Pearson correlation coefficient R. We apply the attenuation operator to the target waveforms for values of t^*_{CAO} between 0–10 in increments of 1 s for both S and ScS as the target signal (since either phase can be more attenuated), and calculate the associated correlation coefficient by allowing the attenuated target waveform to shift in time to maximise similarity with

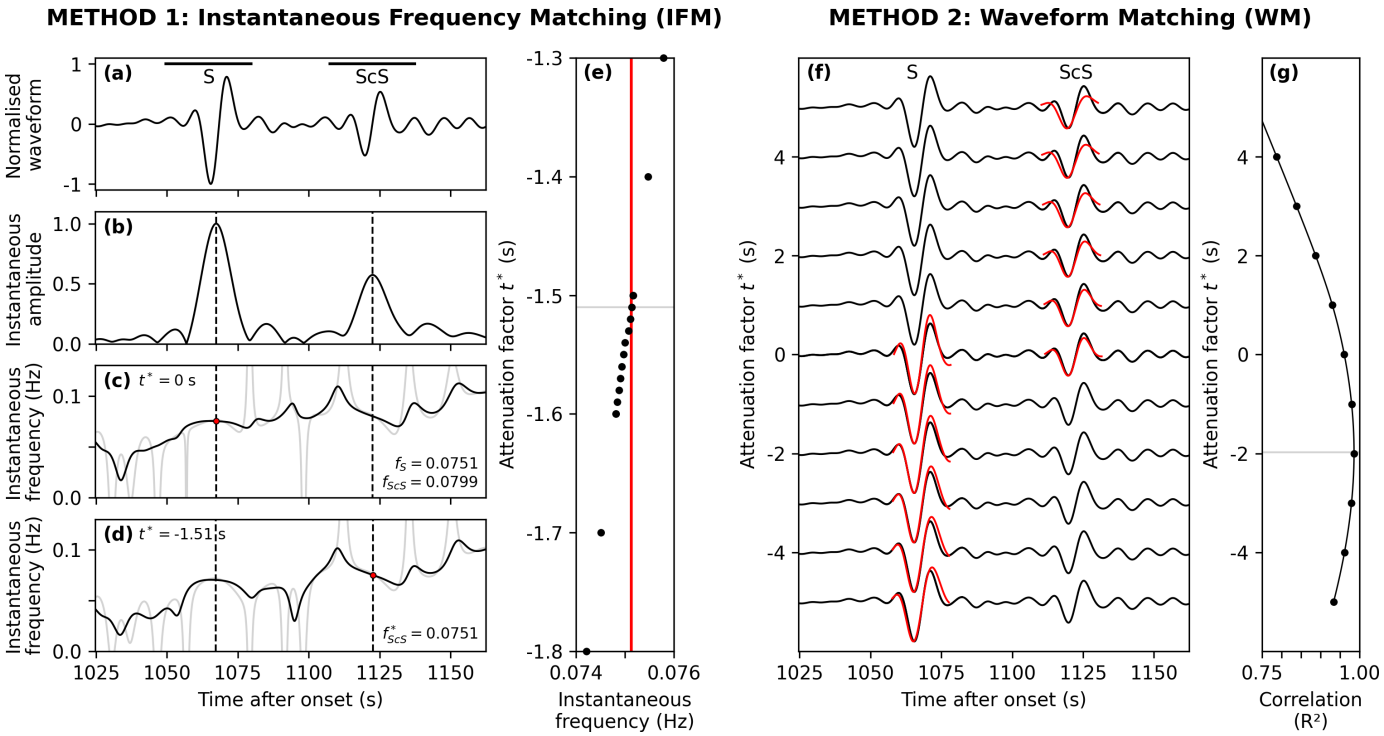

Figure 3: An overview of the two methods used to estimate differential attenuation between S and ScS. Method 1 **(left)** is instantaneous frequency matching (IFM): **(a)** Transverse velocity seismogram for a Mw 6.6 earthquake occurring on 1997/11/28 in South America at 600 km depth, recorded at Southern California Seismic Network station PLM, bandpass filtered between 0.02–0.12 Hz. The black horizontal bar marks a window of ±15 s around the predicted S and ScS arrival times from PREM. The corresponding **(b)** instantaneous amplitude and **(c)** instantaneous frequency of the trace. The dashed lines mark the peaks of instantaneous amplitudes which are used as the reference points to estimate the instantaneous frequencies of S and ScS. The black line is the instantaneous frequency which has been weighted by the instantaneous amplitude, whereas the light grey line is the unweighted instantaneous frequency of the waveform. **(d)** The instantaneous frequency of the trace which has been convolved with the attenuation operator with $t^* = -1.51$. The negative value indicates that S is more attenuated than ScS in this trace. **(e)** A range of values of t^* are trialled iteratively until the instantaneous frequency of the attenuated phase, f^*_{ScS} (black circles), matches the instantaneous frequency of the unattenuated reference phase, f_{S} (red line). Method 2 **(right)** is waveform matching (WM): **(f)** Waveforms which have been synthetically attenuated with different attenuation operator values (red) are overlaid on the original waveforms (black). For positive values of t^*, S waveforms have been attenuated and overlaid on the original ScS waveforms; for negative values of t^*, ScS waveforms have been attenuated and overlaid on the original S waveforms. **(g)** The correlation R^2 between the attenuated and reference signals is calculated for a range of attenuation operator t^* values. The optimum relative attenuation between the two phases can then be estimated from interpolating between these values. The values of $\delta t^*_{\mathrm{ScS\text{-}S}}$ from IFM and WM are -1.51 s and -1.98 s, respectively.

the reference waveform. From this, we then interpolate between the observed correlation coefficients to identify the value of $\delta t^*_{\text{ScS-S}}$ as t^*_{CAO} with the maximum value of R (Figure 3g). Some studies instead jointly determine the relative attenuation, amplitude ratio, time delay and source parameters in a non-linear parameter inversion [e.g. Reid et al., 2001; Garcia et al., 2013; Pejić et al., 2017], but this additional complexity introduces trade-offs which are unnecessary unless the source terms for both phases are not similar.

Assuming that the geometric spreading factor, source radiation pattern, and reflection and transmission coefficients are well known, it is also possible to use a simplified approach to this method of directly inferring δt^* from the envelope ratios of two signals bandpass filtered in a narrow window. For example, this is a commonly used approach to image attenuation in the uppermost inner core from envelope ratios of PKiKP and PKIKP [e.g. Cao and Romanowicz, 2004; Waszek and Deuss, 2013], but has also been used in mantle imaging by comparing envelope amplitudes of S multiples with synthetic waveforms [Zhu et al., 2022] and comparing the amplitude ratios of s to ScS [Zhang et al., 2019]. Hansen et al. [2021] used a similar method to correct for relative attenuation effects between P and PcP waveforms to detect ultra-low velocity zones in the Antarctic region, but did not investigate spatial distributions or patterns of $\delta t^*_{\text{PcP–P}}$ values. Some studies using the spectral ratio method have also used an implicit form of this method to simply verify that the attenuated waveforms (from the attenuation factor determined by spectral division) matched the reference phase better than the unattenuated waveform, and discarded data for which a worse match was recovered, except for low attenuating data for which this requirement is waived [e.g. Fisher et al., 2003; Lawrence and Wysession, 2006].

Whilst waveform matching is less precise than frequency domain methods – which can be seen from the wide range of t^*_{CAO} values that fit the waveforms almost equally well (Figure 3g), compared to the high precision of the instantaneous frequency matching method (Figure 3e) – it is significantly less vulnerable to spectral holes. However, Bhattacharyya [1998] warns that this time domain method can be contaminated by interfering phases resulting in a measurement error of up to 2 s, and that they found frequency domain methods to be more accurate in synthetic tests.

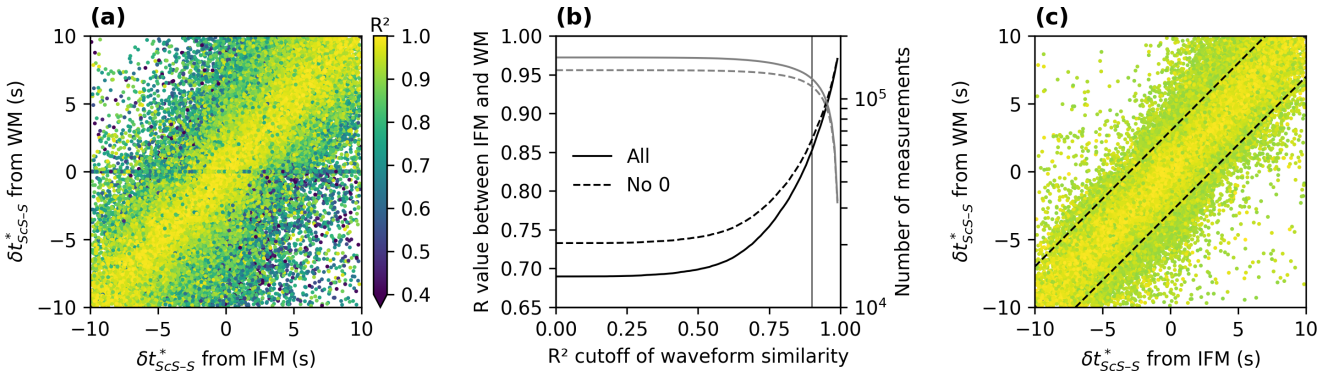

Figure 4: **(a)** A comparison of $\delta t^*_{\text{ScS-S}}$ measurements from the instantaneous frequency matching (IFM) and waveform matching (WM) methods. The colour of the data point corresponds to the correlation R^2 between the waveforms of the original reference phase and the attenuated phase using the value of $\delta t^*_{\text{ScS-S}}$ obtained by the IFM. **(b)** The Pearson correlation value R between the two methods as a function of waveform similarity R^2. **(c)** The dataset for measurements with a waveform similarity of $R_{\text{C}} = 0.9$. The dashed lines are the imposed condition that $\Delta t^* = |\delta t^*_{\text{WM}} - \delta t^*_{\text{IFM}}| < 3$ s.

2.2.4 Combined fitting

We thus opt for a joint fitting approach with the instantaneous frequency matching (IFM) and waveform matching (WM) methods, as recommended by studies that compared frequency and time domain methods [e.g. Der and Lees, 1985; Dasios et al., 2001]. Agreement between the two methods, which have different drawbacks and strengths, significantly increases confidence in the values we obtain. Figure 4a shows the measurements of differential attenuation for IFM and WM, where the points are coloured by the similarity R between the reference and attenuated target waveforms. There are a number of results clustered around $\delta t^*_{\text{IFM}} = 0$ s, due to the way that S and ScS are trialled as the target and reference phases, but these mainly occur for waveforms with low similarity. If we apply additional criteria to our dataset for a minimum similarity R_{C} between the reference and attenuated target waveforms, we find exceptionally good correlation $R_{\text{IFM-WM}} > 0.9+$ between the two methods (Figure 4b-c). Based on this analysis, we set a criteria that $R_{\text{C}} = 0.9$, and we require that the difference between the two methods $\Delta t^* = |\delta t^*_{\text{WM}} - \delta t^*_{\text{IFM}}|$ is less than 3 s (Figure 4c). The measurement of differential attenuation is then taken as the average of the two methods.

Following Ford et al. [2012], we apply a bandpass filter between 0.02–0.12 Hz on the waveforms before estimating attenuation. We then also require that measurements of the weighted instan-

taneous frequencies of S and ScS are between 0.03–0.11 Hz, which removes less than 0.3% of all traces. We take this as evidence that our choice of bandpass preserves the frequency spectra of the data whilst minimising noise.

3 Results

3.1 Preliminary data analysis

We measured δt^* between S and ScS using both IFM and WM (see Methods). Our final dataset is shown in Figure 5 as a function of epicentral distance, separated into six event depth ranges from 75–200 to 600–700 km. The normalised histograms of epicentral distance and differential attenuation are projected onto the top and right hand side axes, respectively. The colours of the dots represent the similarity R between the reference and attenuated target signals. The mean (thick black line) and standard deviation (dashed black line) are plotted for a rolling window of 2° for windows with more than 100 data. The gaps in the data in epicentral distance are due to SS and sS interfering with ScS phases.

The most obvious feature of the data is that there is a significant amount of scatter in the measurements ($\sigma_{\text{noise}} \sim 3$ s) which does not vary with the threshold similarity of waveforms R_{C}. We therefore average the values of differential attenuation and travel time residuals (corrected for attenuation) at the ScS bounce point on a quasi-equal area cell map of the CMB (Figure 6). The travel time residuals show the expected global scale pattern of LLVPs, with ScS raypaths which have travelled through the LLVPs being more delayed relative to S than predicted by PREM (Figure 6b). However, no such large scale features are immediately obvious for the differential attenuation measurements (Figure 6a). We also plot the differential attenuation data separated by turning depth of the S raypath in map view (Figure S7). In this representation, there is a clear global distribution of positive $\delta t^*_{\text{ScS-S}}$ between 800–1000 km (approximately 20–30° epicentral distance), and a clear global distribution of negative $\delta t^*_{\text{ScS-S}}$ for turning depths 1000–2000 km (where 2000 km is the deepest turning depth of S in our dataset). In other words: ScS is more attenuated than S between 20–30° and S is more attenuated than ScS between 30–75°. This matches with the distribution of measured instantaneous frequencies of S and ScS – $f_{\text{S}} = 72.5 \pm 9.1$ mHz and $f_{\text{ScS}} = 73.0 \pm 9.6$ mHz (Figure S8) – that S is more attenuated than ScS on average.

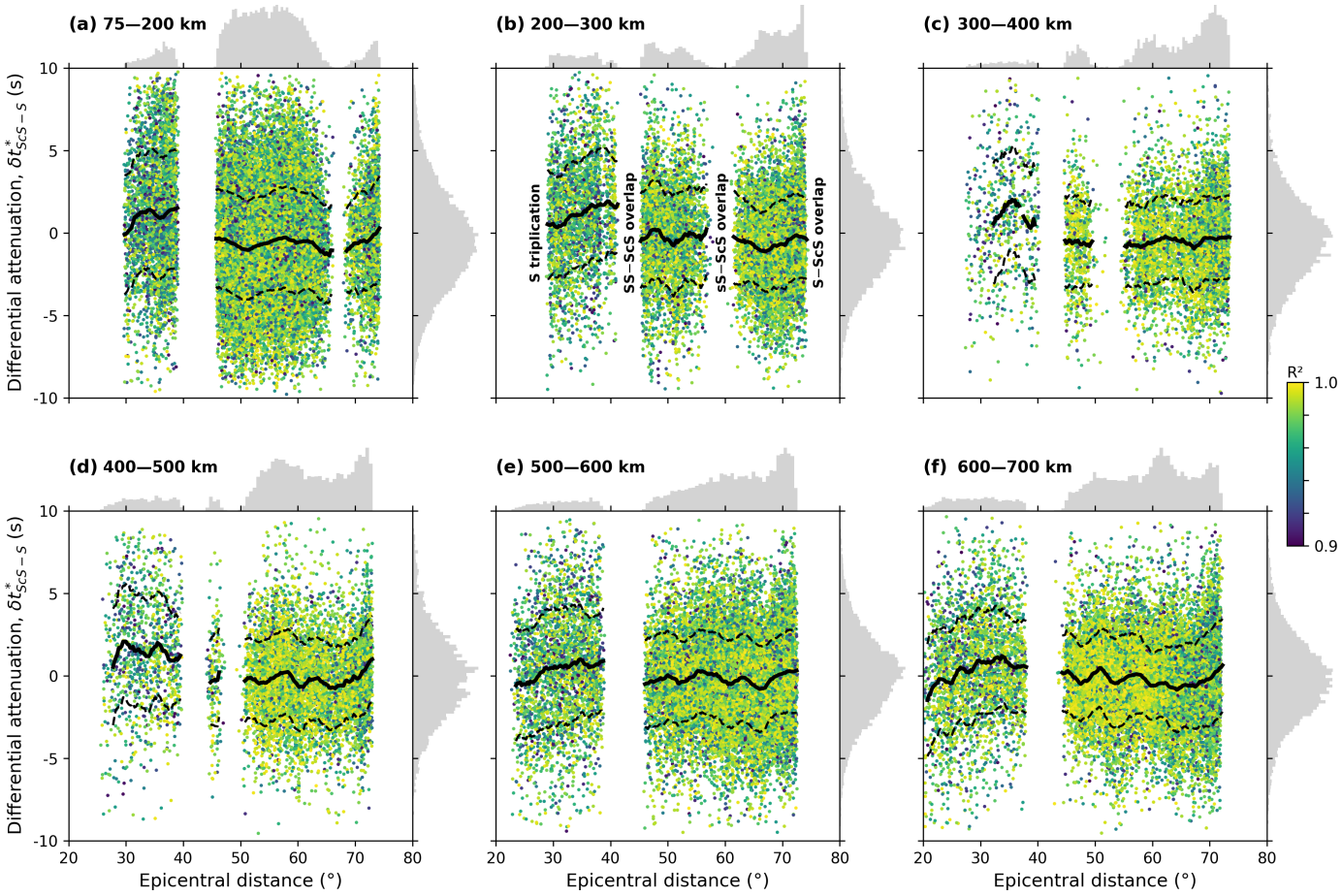

Figure 5: The mean value of differential attenuation $\delta t^*_{\text{ScS-S}}$ between the IFM and WM methods for each waveform within our dataset. The data are plotted in six event depth ranges: **(a)** 75–200, **(b)** 200–300, **(c)** 300–400, **(d)** 400–500, **(e)** 500–600, **(f)** 600–700 km. The colour of each data point is the waveform similarity R^2 between the attenuated phase and the reference phase calculated in the IFM method. The mean (solid black) and standard deviation (dashed black) of each depth range have been overlaid, using a 2° rolling window. Normalised histograms of the epicentral distance and differential attenuation values have been projected on the upper and right sides of the subplots, respectively, for each of the event depth ranges. The gaps in data are a result of SS and sS overlapping with ScS at shorter and longer epicentral distances, respectively.

Before analysing the dataset, we first benchmarked our aggregated observations (Figure 7a) against other published datasets of $\delta t^*_{\text{ScS-S}}$ (Figure 7b). Lai et al. [2019] used waveform matching (WM) of empirical wavelets and Sun et al. [2025] used the instantaneous frequency matching (IFM) method to estimate the absolute attenuation of ScS and S. From these datasets, we then constructed the relative attenuation if both measurements were available at a given event-station pair or epicentral distance. Lawrence and Wysession [2006] used the spectral ratio (SR) method to estimate the relative attenuation of ScS and S, which could be directly compared to our measure-

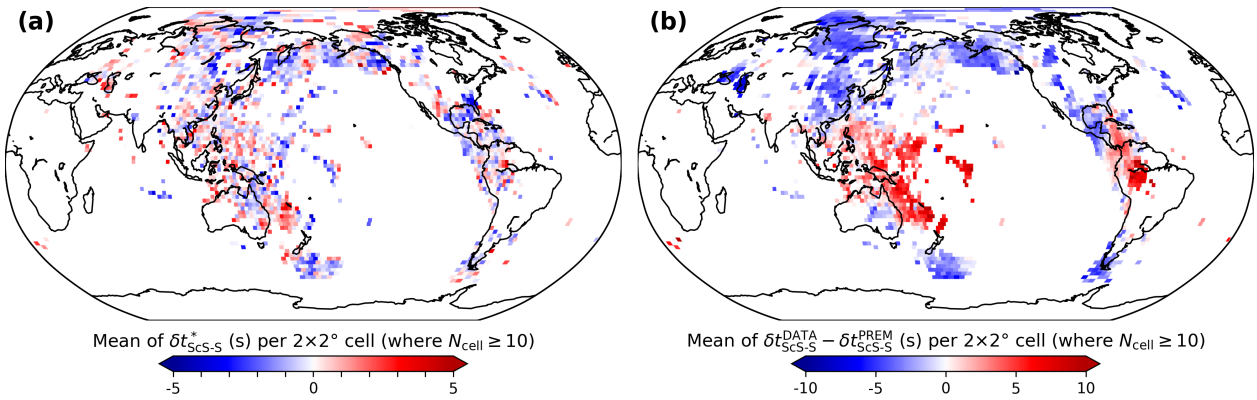

Figure 6: Mean values of **(a)** $\delta t^{*}_{\text{ScS-S}}$ and **(b)** $\delta t^{\text{DATA}}_{\text{ScS-S}} - \delta t^{\text{PREM}}_{\text{ScS-S}}$ per $2 \times 2°$ quasi-equal area cell where grid cells with fewer than 10 ScS bounce points have been omitted.

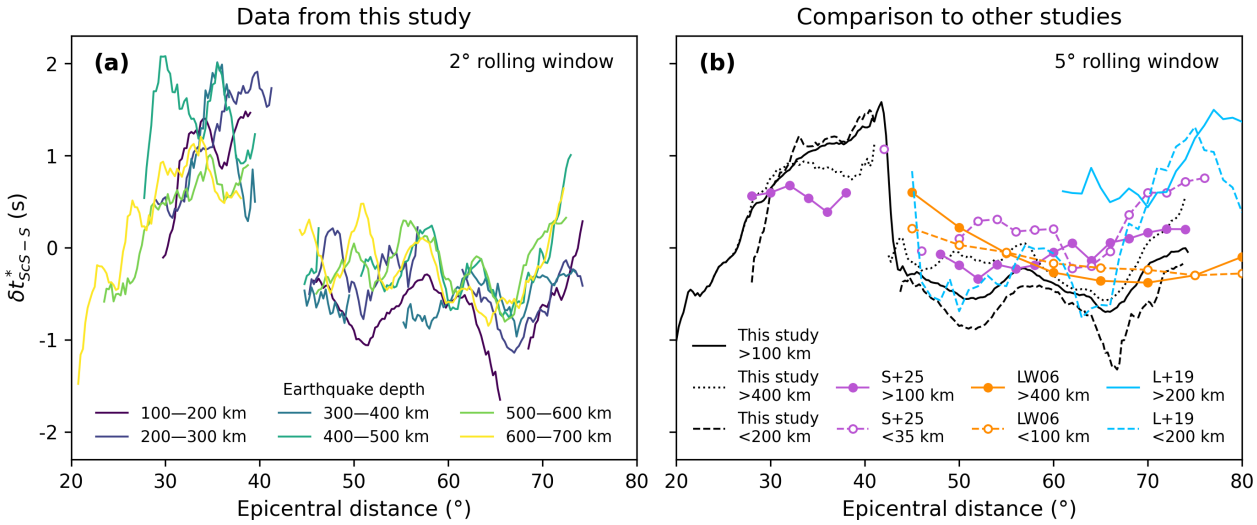

Figure 7: **(a)** The mean value of $\delta t^{*}_{\text{ScS-S}}$ for measurements in this study as a function of epicentral distance and earthquake depth, using a 2° rolling window. **(b)** Comparison of our dataset to other published datasets, using a 5° rolling window. Lawrence and Wysession [2006] made measurements of $\delta t^{*}_{\text{ScS-S}}$ for deep (> 400 km, solid orange) and shallow (< 100 km, dashed orange) earthquakes. Lai et al. [2019] made measurements of absolute attenuation for various phases; where two measurements were made for the same event-station pair, these were binned and averaged in the same way as our dataset but with a minimum threshold of 40 data per bin (blue). A comparison of the $\delta t^{*}_{\text{ScS-S}}$ values constructed from the dataset of Lai et al. [2019] to our dataset is shown in Figure S9. Sun et al. [2025] also made measurements of attenuation for a range of S and ScS multiples relative to PREM; estimates of $\delta t^{*}_{\text{ScS-S}}$ were constructed from the aggregated mean values for each of S and ScS for a 5° rolling window and uncorrected to PREM (purple).

ments, but is also the least consistent with our measurements. Whilst there are differences between the datasets, there are some reassuring similarities: (i) the relative attenuation is more positive at shorter epicentral distances than longer epicentral distances; (ii) there is a consistent increase in relative attenuation between 65–75°; and (iii) a consistent minimum in relative attenuation around 65–70°. However, there are clear offsets in the averages between datasets and also in the amplitude of our dataset compared to the others. It is difficult to ascertain whether this is due to lateral variations in the data sampling distributions or accuracy of the measurement techniques used in the studies, or both.

3.2 Forward modelling

Since measurements of $\delta t^*_{\text{ScS-S}}$ represent the cumulative attenuation difference between two raypaths, interpreting the data is not a straightforwardly intuitive process. Our first step was therefore to perform forward modelling to establish how variations in Q_μ influence the predicted $\delta t^*_{\text{ScS-S}}$. Figure 8 shows how perturbations in Q_μ in different depth layers affect the predicted $\delta t^*_{\text{ScS-S}}$ as a function of epicentral distance. At shallow depths, from the surface to ∼750 km depth, there is very little deviation from a uniform Q_μ for strong positive or negative perturbations due to the negligible difference between the S and ScS raypaths. Towards the bottom of the mantle, below ∼2200 km depth, positive and negative perturbations in layers of the uniform Q_μ profile result in approximately linear negative and positive shifts in $\delta t^*_{\text{ScS-S}}$, respectively. This occurs due to ScS spending approximately the same time at each depth, which varies little with epicentral distance. However, at intermediate depths, between ∼750–2200 km, there are strong non-linear effects, with some epicentral distance ranges shifted positively and others shifted negatively. We thus refer to our final model, which is a 1D model with sensitivity mostly to the mid-mantle region, as Q_{M1D}. The relationship between the $Q\mu$ profile with depth and resulting $\delta t^*_{\text{ScS-S}}$ with epicentral distance can therefore be approximately interpreted as a direct mapping, since the depth in the Q_μ profile is largely determined by the turning depth of the S raypath.

We include epicentral distances less than 40° despite potential triplication of S arrivals, as the waveforms are not strongly affected by this effect [e.g. Wang et al., 2018]. Since we require WM and IFM to produce similar values, $|\delta t^*_{\text{IFM}} - \delta t^*_{\text{IFM}}| < 3$ s, and the attenuated waveform matches the unattenuated reference waveform, $R_{\text{C}} = 0.9$, this effect has a negligible effect on our dataset. We

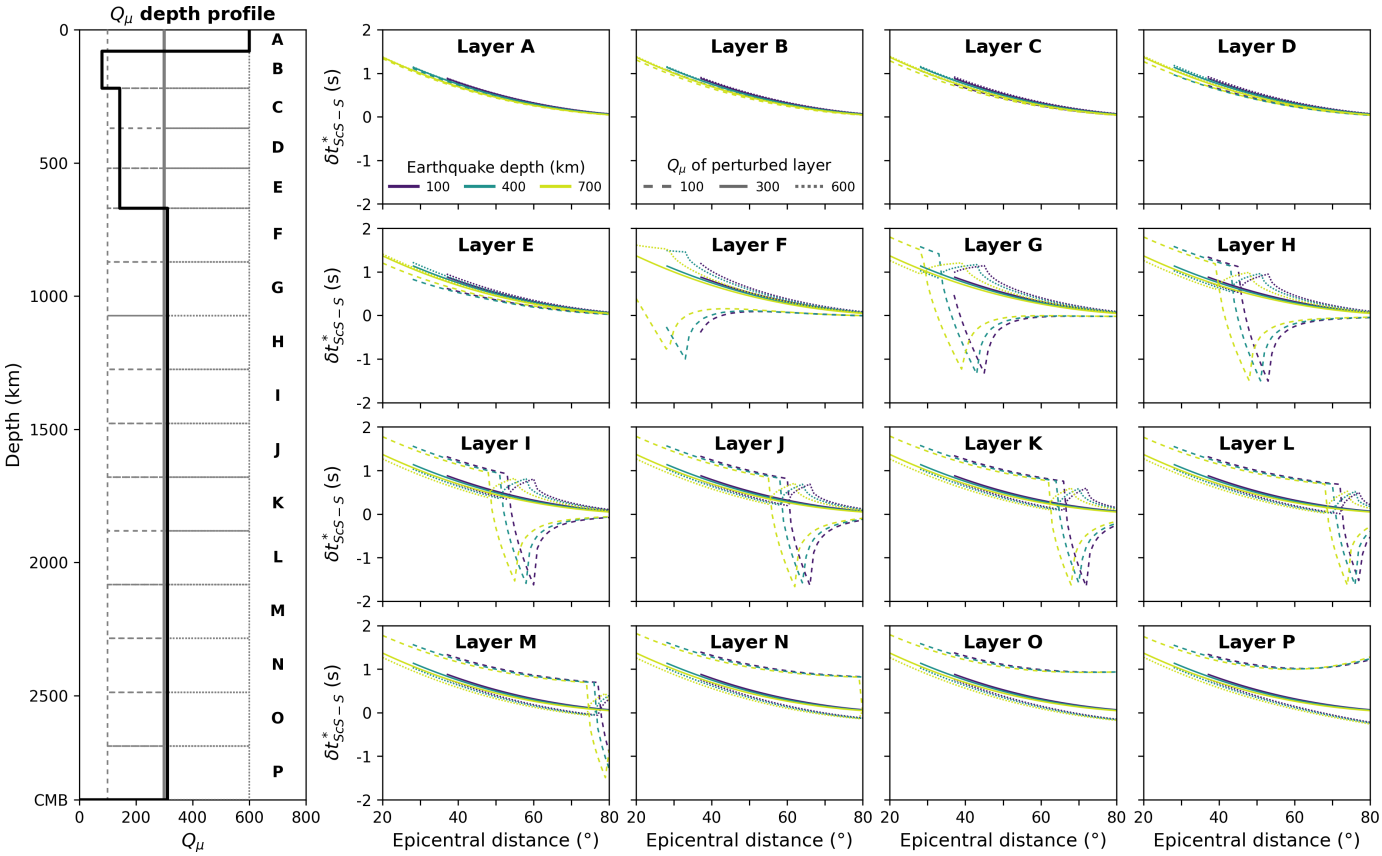

Figure 8: A depth profile **(left)** has been split up into 16 approximately equal depth ranges and labelled **Layers A–P**. The Q_μ profile for PREM is plotted for reference. Subplots **(right)** show the predicted $\delta t^*_{\text{ScS-S}}$ profiles as a function of epicentral distance for a perturbation in each layer only. The value of Q_μ in all other depth ranges is kept at 300. Each perturbed layer is allowed the value of 100 (dashed) or 600 (dotted), which is compared to a uniform profile of $Q_\mu = 300$ (solid).

also visually inspected S waveforms in this epicentral distance range for several events to confirm this. At epicentral distances much longer than 75°, the separation between S and ScS waveforms in the seismograms becomes too small to robustly interpret.

3.3 Inversion for 1D Q_μ

We next perform an inversion for 1D Q_μ, in which we compute the forward model for earthquakes depths of 100 to 700 km in intervals of 50 km and epicentral distances of 20 to 80° in intervals of 0.5°. We then compute the misfit by comparing the measured $\delta t^*_{\text{ScS-S}}$ with the model corresponding to the nearest depth and distance of the event-station pair for the measurement. Before the inversion, we pre-compute the raypaths of S and ScS using TauP [Crotwell et al., 1999] through ObsPy [Beyreuther et al., 2010] for PREM, which makes each computation of the forward model extremely

efficient. One full iteration – to compute $13 \times 121 = 1573$ forward models and the corresponding misfit for 100,000 measurements – takes on the order of 0.5 s on a single processor. As such, it becomes feasible to perform a Markov chain Monte Carlo (McMC) inversion which is able to explore a wide parameter space and, most importantly, robust estimates of the associated uncertainties [e.g. Bodin and Sambridge, 2009].

We parameterise the Q_μ profile as a function of cubic B-splines in depth, such that

$$Q_\mu(r) = \sum_k p_k f_k(r) \tag{11}$$

where $f_k(r)$ are the cubic B-splines functions at radius r and p_k are the corresponding weighting factors of the basis functions. Since the weights of cubic B-splines are strictly positive, it means that all Q_μ profiles will be positive for $p_k > 0$. We thus allow p_k to vary between 1 and 1000 (the prior distribution). From our initial analysis of the data, we expect a strongly heterogeneous region between 500–1000 km depth where our data shows strong variability. As such, we chose to use basis functions with 32 depth knots to ensure adequate depth resolution. We set the uppermost 400 km knots with fixed separation of 50 km with p_k chosen to be PREM-like, with the remaining knots distributed such that the spacing between nodes increases linearly down to the CMB (Figure 9a).

The misfit $\Phi(m)$ of a model m of Q_μ is defined as

$$\Phi(m) = \sum_i \left(\frac{p_i(m) - d_i}{\sigma_{\text{noise}}} \right)^2 \tag{12}$$

where p is the predicted value of $\delta t^*_{\text{ScS-S}}$ for the model m, d is the observed value of $\delta t^*_{\text{ScS-S}}$, and σ_{noise} is the estimated value of the data noise (chosen as 5 s). This is larger than the standard deviation of the overall dataset of $\delta t^*_{\text{ScS-S}}$ measurements ($\sigma_{\text{noise}} \sim 3$ s), but this was chosen to ensure the parameter space was well explored in a manner similar to simulated annealing [e.g. Weber, 2000]. For a proposed model m', one randomly chosen weighting factor is perturbed by a step length drawn from a Gaussian distribution, $p'_k = p_k + \Delta p_k$. The forward model scheme is then run for the 1573 combinations of event depth and station epicentral distance using the proposed model, and the misfit is calculated for the dataset. The natural logarithm of the acceptance probability is [e.g.

Bodin and Sambridge, 2009]

$$\ln\left[\alpha\left(m'\middle|m\right)\right] = \min\left[0, \tfrac{1}{2}\left(\Phi(m') - \Phi(m)\right)\right] \tag{13}$$

The acceptance probability is then compared to a randomly drawn value $w = [0, 1)$: if $\alpha > w$ the proposed model m' is accepted, otherwise it is rejected and a new proposal is made from the current model m. The form of the acceptance probability means that all proposed models which decrease the misfit are accepted, whilst those which increase the misfit can sometimes be accepted depending on the value of w. The posterior distribution, the probability distribution of Q_μ profiles which fit our dataset, is then taken to be the sparsely sampled distribution of models m after a sufficient burn in period to remove transient effects of the starting conditions [e.g. Bodin and Sambridge, 2009]. We find that for the setup presented here – 32 depth knots with the upper 6 fixed to PREM-like values – the inversion converges after a burn in period of $\sim$2000 iterations. The inversion ensemble is then taken as every 500th iteration from 50 parallel inversions after a burn in period of 2500 iterations and run for 12000 iterations. The ensemble distribution therefore comprises of 1000 uncorrelated models from the posterior distribution, from which we calculate the mean and standard deviation in each of the weighting factors p_k.

We also explored a range of other inversion setups, including:

1. Changing the number of depth knots and their relative separation (Figures S11 & S12). We found that, regardless of the number of knots, the resulting Q_μ profile is very consistent although the profiles with fewer knots led to broader features. 32 depth knots was a balance between sufficient depth resolution and minimising overfitting noise.

2. Parameterising Q_μ in logarithmic space, similar to parameterisation used by Sun et al. [2025]. However, we found that unless we used a large number of depth splines that this parameterisation was less stable due to the strong variations in Q_μ required to fit our observed data.

3. Adding additional terms to the misfit if the predicted values of values of absolute attenuation t^*_S were higher than those of PREM. This test was a result of recent measurements of absolute attenuation of t^*_S which were approximately equal to or less attenuating than PREM synthetics

across all measured epicentral distances [Zhu et al., 2022; Sun et al., 2025].

4. Using different starting models to initiate the inversion. Due to the relatively high value of σ_{noise} we use, the inversion was always well converged by ∼2000 iterations for any uniform starting models of Q_μ between 100–800.

Our final model, Q_{M1D}, is taken as the mean of the distribution of Q_μ profiles in the inversion ensemble, shown in Figure 9b, with the associated uncertainty in the model taken as the uncertainty in the weighting factor of each depth knot. Our model shows a strongly attenuating layer ($Q_\mu < 100$) at 750 km depth and two weakly attenuating layers ($Q_\mu \sim 600$) at 900 and 2000 km depth. Between the two weakly attenuating layers, the mid-mantle is relatively strongly attenuating ($Q_\mu \sim 150 - 250$). We then also compare our model to some previously published models (Figure 9c-d): PREM [Dziewonski and Anderson, 1984], QM1 [Widmer et al., 1991], QL6 [Durek and Ekström, 1996], QDW14 [De Wit et al., 2014], REM1D [Moulik and Ekström, 2025], QS4L3 [Talavera-Soza et al., 2025], QLM9 [Lawrence and Wysession, 2006], QHR11 [Hwang and Ritsema, 2011], QMSF [Zhu et al., 2022] and Q_{L1D} [Sun et al., 2025]. PREM, QM1, QL6, QDW14, REM1D and QS4L3 are constructed from measurements of attenuation of normal modes; whilst QLM9, QHR11, QMSF, Q_{L1D} and Q_{M1D} are from measurements of attenuation of body waves. Predictions of $\delta t^*_{\text{ScS-S}}$ for these Q_μ profiles are plotted against the average of our measurements, which show that only Q_{M1D} matches the trends in our dataset (Figure 10).

3.4 Comparison with other body wave lower mantle models

Our model Q_{M1D} differs significantly from previous models, notably around 500–1000 km depth. Whereas Zhu et al. [2022] and Sun et al. [2025] observe a weakly attenuating region around 750 km depth, our model prefers a thin strongly attenuating layer. There are also two very distinct low attenuation layers around 900 and 2000 km depth, the latter of which is not seen in any of the other models. These features in the Q_μ profile result in a significantly better fit to our dataset of $\delta t^*_{\text{ScS-S}}$ measurements than any of the other models, which are broadly flat across the epicentral distance range (Figure 10).

As well as direct comparisons between our observations of $\delta t^*_{\text{ScS-S}}$ with those from other studies (Figure 7), we also compared our model Q_{M1D} to observations of other differential phase pairs,

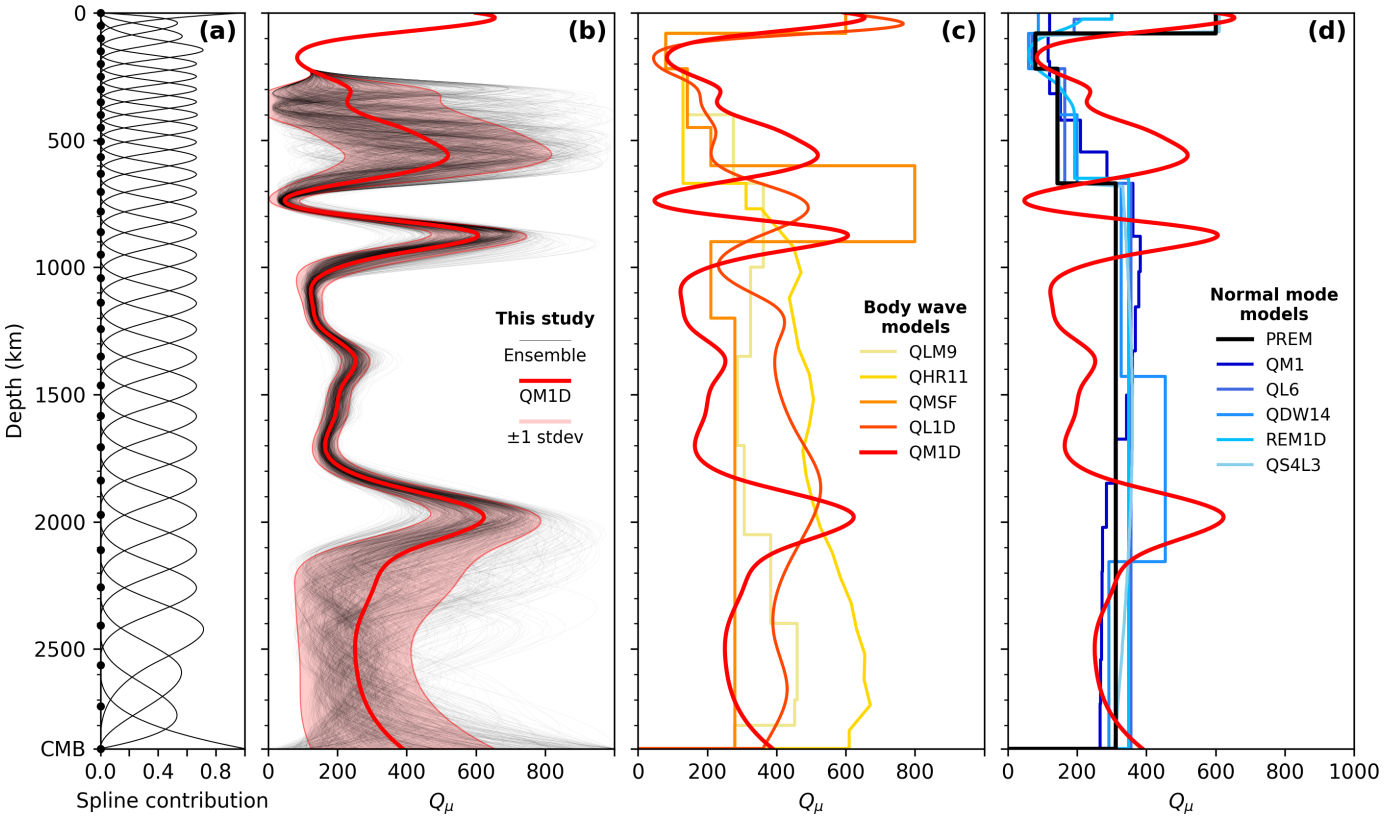

Figure 9: **(a)** The cubic B-splines of the basis functions used in our modelling with 32 depth knots. **(b)** The ensemble of models from our inversion (thin black lines), with the mean and standard deviation of the ensemble (red and pink, respectively). The mean of the ensemble is taken to be our model Q_{M1D} with its corresponding uncertainties for each depth parameter. A comparison of our model with **(c)** other short period body wave models (warm colours) and **(d)** various long period normal mode models (cool colours) of shear attenuation: black [PREM, Dziewonski and Anderson, 1984], dark blue [QM1, Widmer et al., 1991], blue [QL6, Durek and Ekström, 1996], medium blue [QDW14, De Wit et al., 2014], sky blue [REM1D, Moulik and Ekström, 2025], light blue [QS4L3, Talavera-Soza et al., 2025], pale yellow [QLM9, Lawrence and Wysession, 2006], yellow [QHR11, Hwang and Ritsema, 2011], orange [QMSF, Zhu et al., 2022], dark orange [Q_{L1D}, Sun et al., 2025], red [Q_{M1D}, this study].

SS-S and SSS-SS (Figure S10c-d). Predictions from Q_{M1D} for these observations show a distinctly poor match, which is likely due to the poor resolution of the shallow mantle by the dataset we used to construct our model, but also due to the unmatched upper mantle and crustal contributions to the measurements for the differential phases. Similarly, several studies have found that their observations of attenuation are less attenuating than PREM in contradiction with our results (Figure S10e-g). Zhu et al. [2022] find that, on average, the amplitudes of SS, SSS and SSSS phases are larger than those predicted in synthetics of PREM, implying that any model should be less

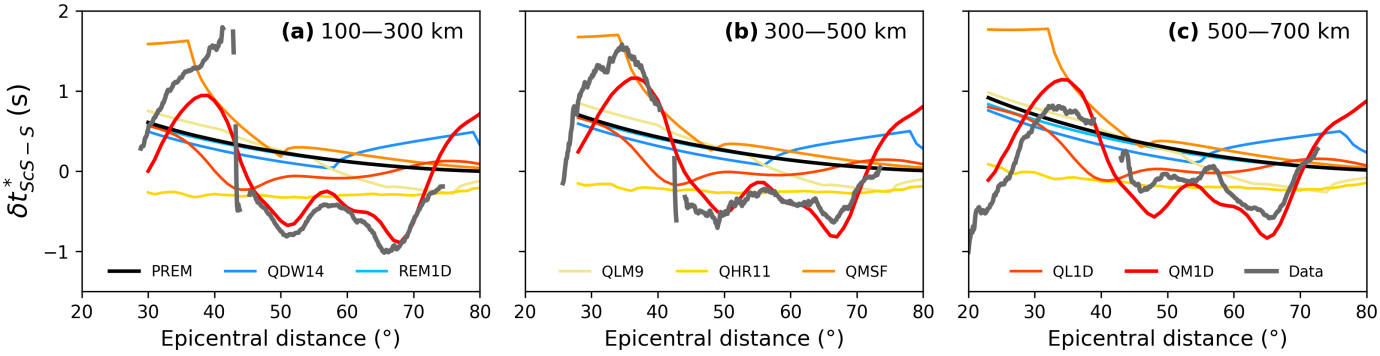

Figure 10: A comparison of predictions and observations of $\delta t^*_{\text{ScS-S}}$ for a few different Q_μ profiles from Figure 9. Averaged $\delta t^*_{\text{ScS-S}}$ measurements are shown for event depth ranges **(a)** 100–300, **(b)** 300–500 and **(c)** 500–700 km, using a 5° rolling window (grey lines).

attenuating than PREM overall. Hwang and Ritsema [2011] similarly found that their t^*_{data} was consistently below the predicted value of t^*_{PREM} for P and S waves. More recently, a similar analysis on a larger scale was completed by Sun et al. [2025] for S, SS, SSS, SSSS, ScS, ScS_2, ScS_3, Sdiff, and their respective depth phases. Whilst again there was a significant scatter in the data, there was a consistent trend that the phases were less attenuated than predicted by PREM. Sun et al. [2025] also suggested that there may be a low attenuation layer around 2000 km depth (although this is not clear from model Q_{L1D}). Indeed, adding a more pronounced low attenuation layer in their preferred model Q_{L1D} at this depth improves the fit to their dataset of t^*_{SS} measurements (Figure S10f).

Our model Q_{M1D} would also have important implications for assumptions in previous studies, which invert for attenuation in the upper mantle using the assumption that the lower mantle contributes negligible attenuation [e.g. Warren and Shearer, 2002; Souriau et al., 2012; Nguyen et al., 2025]. Several studies have also assumed that a smoothly varying velocity profile from the base of the mantle transition zone to the top of the D" region implies lack of strong attenuation heterogeneity in this region [e.g. Flanagan and Wiens, 1994]. Our model therefore suggests caution to future studies who assume the effect of attenuation in the lower mantle can be neglected.

Zhao et al. [2015] investigated the Pacific region by creating an empirical source function for and comparing the broadening of S. On average, as a function of epicentral distance, the S waves which turning within the lowermost 900 km were more attenuating than S waveforms which turned around 900 km. This matches with our observation of a low attenuation region around 2000 km

(approximately 900 km above the CMB) with stronger attenuation below this region. This could suggest that our observation of a low attenuation layer at 2000 km depth may be a globally present feature, rather than just around the Pacific where our dataset is spatially biased.

3.5 Comparison with normal mode models

Nearly all Q_μ profiles derived from long period normal mode measurements of attenuation feature a roughly uniform low attenuating lower mantle with Q_μ between 300–400 [e.g. Dziewonski and Anderson, 1981; Moulik and Ekström, 2025], except for QR05 [Resovsky et al., 2005] and QDW14 [De Wit et al., 2014] which suggest that there is a weakly attenuating layer between 1500–2000 km depth. In our model, we find a more strongly attenuating mid-mantle (Q_μ=150–250), flanked by two regions of low attenuation (Q_μ =500–700). Given the poor depth resolution of normal modes [e.g. Talavera-Soza et al., 2025], most models are constructed using a very coarse parameterisation of the lower mantle, with the notable exception of QM1 [Widmer et al., 1991]. It is therefore plausible that the weakly attenuating layer observed by Resovsky et al. [2005] and De Wit et al. [2014] is the same as the one we find around 2000 km depth. The lowermost 600 km of the mantle in our model is also consistent with the long period Q_μ profiles, although we note that Q_{MID} is poorly constrained in this region and there is a large uncertainty in our model (Figure 9b). Finally, there do not appear to be any similarities between normal mode models and the more attenuating mid-mantle in Q_{M1D} or for the weakly attenuating layer at 900 km depth.

Attenuation is generally considered to be frequency dependent, i.e. $Q = Q_0 f^\alpha$ [e.g. Anderson and Given, 1982], with a value of $\alpha \sim 0.1-0.3$ derived seismically [e.g. Lekić et al., 2009; Zaroli et al., 2010; Romanowicz and Mitchell, 2015] and experimentally [e.g. Jackson and Faul, 2010; McCarthy et al., 2011]. Over narrow frequency ranges, it is typically assumed that attenuation is frequency independent – for example, this is an assumption of the spectral ratio method – although Moulik and Ekström [2025] find that they do not need to invoke frequency dependence of attenuation to satisfy observations over the range 1–3200 s, i.e. $\alpha = 0$. If attenuation is frequency dependent, $Q\mu$ measured from body waves (higher frequency) would be expected to be higher than those from normal modes (lower frequency) [e.g. Hwang and Ritsema, 2011; Sun et al., 2025]. In the layer of low attenuation and in lowermost mantle, $\alpha = 0.19 - 0.28$ and $\alpha \sim 0$, respectively. However, we find that the observed Q_μ in the mid-mantle is lower than that of PREM, which would suggest a

negative value of $\alpha = -0.13 - 0.20$.

4 Discussion

4.1 Uncertainty in the data and methodology

Various effects – discussed below – can cause an increase in observed or 'apparent' attenuation, which is therefore always larger than the true or 'intrinsic' attenuation.

4.1.1 Effect of de/focussing of elastic structure

Chaves and Ritsema [2016] demonstrated using synthetic modelling that measurements of ScS/ScS_2 amplitude ratios are dominated by focussing effects rather than 3D variations in attenuation. Similarly, Pang et al. [2023] found that focussing effects accounted for up to 20% of the differential attenuation between station pairs of shallow events measured using the spectral ratio method. However, they noted that the complex azimuthal patterns observed in shallow events were almost non-apparent for events deeper than 150 km.

At short epicentral distances, the layered velocity structure in the upper mantle results in triplication of S. This would also likely lead to broadening of the S waveform and an apparent increase in t^*_{S} and a more negative $\delta t^*_{\mathrm{ScS\text{-}S}}$, which matches the trend in relative attenuation we observed (Figure 5). However, this appears to be a robust trend across all event depths and extends well into epicentral distances for which triplications are not predicted (models are truncated in Figure 10 when triplications are predicted in PREM). Additionally, the number of measurements at the shortest epicentral distances are far outnumbered by those at longer epicentral distances (Figure 5) and so any trend in the data will have a weak effect on the misfit during the inversion process. Nonetheless, we only include data in the misfit for which PREM does not predict a triplication in S, resulting in a final dataset of 94,000 $\delta t^*_{\mathrm{ScS\text{-}S}}$ measurements from 894 events.

4.1.2 Effect of anisotropy

Presence of anisotropy in the mantle can also lead to the broadening of the SH phase, which could be interpreted as due to anelastic attenuation [Cormier, 2020]. In the mantle, anisotropy is thought only to be significant in the uppermost and lowermost mantle. Since S and ScS have similar paths

near to the receiver, any potential broadening would affect both phases and approximately cancel out. However, only ScS passes through the lowermost mantle and so it is possible that there is a small contribution to broadening of ScS, resulting in a larger apparent differential attenuation between ScS and S (i.e. more positive $\delta t^*_{\text{ScS-S}}$). When we compare our dataset with other published values, we find that our average values of $\delta t^*_{\text{ScS-S}}$ are in fact more negative. Therefore, it us unlikely that anisotropy affects our dataset noticeably. Indeed, Ford et al. [2012] and Durand et al. [2013] – who both investigated the effect of correcting for anisotropy on measurements of deep earthquakes targetting the CMB near Central America – concluded that the effect was small (on the order of tenths of a second) and that corrections did not correlate with 3D velocity models. As such, we do not correct for any potential splitting caused by anisotropy in this study.

4.1.3 Effect of scattering

Elastic structure on the order of wavelength of the seismic waves can cause the elastic redistribution (scattering) of energy which results in an effective pulse broadening and increase in apparent attenuation [e.g. Cormier, 2020]. Such scatterers could explain attenuation, but would require significant variations in density and elastic parameters of 6–9% which is much larger than observed in tomographic models [Ricard et al., 2014]. Small-scale structure may be present in the mid-mantle [e.g. Kaneshima, 2016; Waszek et al., 2018], which would result in more scattering of S than ScS on average and therefore lead to the more negative values of $\delta t^*_{\text{ScS-S}}$ we observe. However, most seismic observations of scatterers have been located within or near the D" layer in the lowermost mantle [e.g. Shearer, 2007; Rost et al., 2015; Rost and Frost, 2025]; there are few studies which suggest there are small-scale scatterers in the mid-mantle. Therefore, since scatterers in the D" would only affect ScS which would result in a more negative $\delta t^*_{\text{ScS-S}}$, it seems unlikely that scattering has had a significant impact on our measurements. Various studies have attempted to distinguish between intrinsic attenuation and scattering from apparent attenuation using radiative transfer theory [e.g. Fehler et al., 1992; Carcolé and Sato, 2010; Ogiso, 2019; Akande et al., 2019], but this is beyond the scope of this paper.

4.2 Comparison to mineralogy

Whilst in the upper 400 km of the mantle there is increasing evidence for an anti-correlation between shear velocity and attenuation [e.g. Romanowicz, 1995; Dalton et al., 2008; Karaoğlu and Romanowicz, 2018; Talavera-Soza et al., 2025] – suggestive of related causal physical mechanisms such as temperature, grain size, water content or partial melt [e.g. Jackson et al., 2002] – there does not appear to be any similar correlation between 1D models of shear velocity and attenuation in the lower mantle. We compared the observations of differential attenuation $\delta t^*_{\text{ScS-S}}$ with 3D tomographic models SEMUCB-WM1 [French and Romanowicz, 2014], REVEAL [Thrastarson et al., 2024] and GLAD-M35 [Cui et al., 2024] for shear velocity at the turning point of S (Figure S13) and at the bounce point of ScS (Figure S14) of our dataset. There is a weak anti-correlation between shear velocity at the turning point of S with differential attenuation ($R \sim -0.08$) and a weaker anti-correlation between shear velocity at the bounce point of ScS with differential attenuation ($R \sim -0.03$). The strongest – but still weak – anti-correlation is found between the double difference travel time and differential attenuation (Figure S15, $R \sim -0.09$).

Previous studies have interpreted low attenuation layers in their Q_μ profiles as evidence for regions of high viscosity [Lawrence and Wysession, 2006; Sun et al., 2025]. Several studies have found evidence for an increased viscosity in the mantle around 1000 km depth from geodynamical modelling [e.g. Kido and Čadek, 1997; Forte and Mitrovica, 2001; Höink et al., 2012; Rudolph et al., 2015] and experimental mineralogy [e.g. Marquardt and Miyagi, 2015]. Forte and Mitrovica [2001] additionally identified an increase in viscosity around 2000 km depth, matching our observation of a low attenuation layer at this depth, which Glišović et al. [2015] interpreted as the region of maximum grain size within the mantle. The thin highly attenuating layer in our model at 750 km depth is also consistent with previous suggestions of a thin low viscosity layer at the bottom of the MTZ which controls slab stagnation [e.g. Mitrovica and Forte, 2004; Mao and Zhong, 2018].

4.3 Future developments and suggestions

ScS-S is fundamentally limited by the source-receiver geometries for which ScS can be measured without being contaminated by other phases (Figure 1), resulting in a spatial sampling biased around the edge of the Pacific (Figure 2). Other studies which have addressed the problem of

spatial bias have typically measured absolute attenuation values of different shear phases [e.g. Lai et al., 2019; Zhu et al., 2022; Sun et al., 2025]. However, measuring the absolute attenuation is difficult and involves strong assumptions about the attenuation contributions from the source and receiver regions [Sun et al., 2025]. As such, other pairs of differential phases are required to increase the spatial sampling and ensure less uncertainty in measurements of δt^*. ScSScS and SS may be one such potential avenue to increase the spatial sampling of our dataset. Whilst, this phase combination will still have the same constraints of depth sensitivity – i.e. predominantly the mid-mantle – it would be more globally representative than the spatially biased $\delta t^*_{\text{ScS-S}}$ dataset we currently have. Such improvements in spatial sampling are required to make progress towards a 3D model of attenuation of the mantle from body waves.

Figure S11 shows the inversion results for a number of different depth splines with 24, 32, 50 and 90 knots. We recommend any future study using a spline parameterisation for Q_μ to use an irregularly spaced arrangement of knots to ensure good resolution around the 900 and 2000 km layers of low attenuation. Alternatively, it may be preferable to perform a transdimensional McMC in which the number of knots is also an unknown variable [e.g. Bodin and Sambridge, 2009], but this would create additional challenges if the objective is a 3D model of attenuation computationally feasible.

5 Summary

Using a dataset of 94,000 high-quality measurements of differential attenuation between S and ScS body waves, we have constructed a new 1D model of shear attenuation Q_μ in the mantle, Q_{M1D}. We find a strongly attenuating layer around 750 km depth, and two weakly attenuating layers at 900 and 2000 km depth. We speculate that the distinct low attenuation layers at 900 and 2000 km depth could be related to subducted slabs and an increase in global viscosity in the deep mantle, respectively. Our model also suggests the mid-mantle is more attenuating than usually assumed from normal modes.

Acknowledgements

CM and AD were funded by a Vici award (grant number 016.160.310/526) from the Dutch Research Council (NWO). The computational facility at Utrecht, Eejit, was used to perform the analysis in this work. We thank Hanneke Paulssen, Stuart Russell, Jochem Veerman, Michael Koch and Lauren Waszek for helpful discussions and Lukas van de Wiel for technical support. We used TauP [Crotwell et al., 1999] and ObsPy [Beyreuther et al., 2010] to do the analysis in this project, and matplotlib [Hunter, 2007] and basemap (https://matplotlib.org/basemap/) to make the figures.

Data and code availability

The facilities of IRIS Data Services (www.iris.edu), and specifically the IRIS Data Management Center, were used for access to waveforms and related metadata. IRIS Data Services are funded through the Seismological Facilities for the Advancement of Geoscience (SAGE) Award of the National Science Foundation under Cooperative Support Agreement EAR-1851048. Data from the TA network were made freely available as part of the EarthScope USArray facility, operated by Incorporated Research Institutions for Seismology (IRIS) and supported by the National Science Foundation, under Cooperative Agreements EAR-1261681. Earthquake parameters were used from the Global CMT Project (www.globalcmt.org). Codes and datasets will be made available on Zenodo upon publication.

Competing interests

Authors declare that they have no competing interests.

References

Adenis, A., Debayle, E. and Ricard, Y. [2017], 'Attenuation tomography of the upper mantle', **44**(15), 7715–7724.

Akande, W. G., De Siena, L. and Gan, Q. [2019], 'Three-dimensional kernel-based coda attenu-

ation imaging of caldera structures controlling the 1982-84 Campi Flegrei unrest', *Journal of Volcanology and Geothermal Research* **381**, 273–283.

Aki, K. and Richards, P. G. [2002], *Quantitative seismology*, MIT Press.

Anderson, D. L. and Given, J. W. [1982], 'Absorption band Q model for the Earth', *Journal of Geophysical Research: Solid Earth* **87**(B5), 3893–3904.

Asada, T. and Takano, K. [1963], 'Attenuation of short period P waves in the mantle', *Journal of Physics of the Earth* **11**(1), 25–34.

Barnes, A. E. [1993], 'Instantaneous spectral bandwidth and dominant frequency with applications to seismic reflection data', *Geophysics* **58**(3), 419–428.

Bernard, P., Herrero, A. and Berge, C. [1996], 'Modeling directivity of heterogeneous earthquake ruptures', *Bulletin of the Seismological Society of America* **86**(4), 1149–1160.

Beyreuther, M., Barsch, R., Krischer, L., Megies, T., Behr, Y. and Wassermann, J. [2010], 'ObsPy: A Python toolbox for seismology', *Seismological Research Letters* **81**(3), 530–533.

Bezada, M. J., Byrnes, J. S., Zhu, Z. and Lee, H. [2023], 'Lateral Variations in Teleseismic Attenuation of the Conterminous U.S. and New Insights Derived From Its Relationship to Mantle Seismic Velocity', *Journal of Geophysical Research: Solid Earth* **128**(12), e2023JB027299.
URL: *https://agupubs.onlinelibrary.wiley.com/doi/abs/10.1029/2023JB027299*

Bhattacharyya, J. [1998], 'Comparison between time-domain and frequency-domain measurement techniques for mantle shear-wave attenuation', *pure and applied geophysics* **153**(2), 399–417.

Bhattacharyya, J., Masters, G. and Shearer, P. [1996], 'Global lateral variations of shear wave attenuation in the upper mantle', *Journal of Geophysical Research: Solid Earth* **101**(B10), 22273–22289.

Bodin, T. and Sambridge, M. [2009], 'Seismic tomography with the reversible jump algorithm', *Geophysical Journal International* **178**(3), 1411–1436.
URL: *https://doi.org/10.1111/j.1365-246X.2009.04226.x*

Borgeaud, A. F. and Deschamps, F. [2021], 'Seismic Attenuation and S-Velocity Structures in Beneath Central America Using 1-D Full-Waveform Inversion', *Journal of Geophysical Research: Solid Earth* **126**(7), e2020JB021356.

Brune, J. N. [1970], 'Tectonic stress and the spectra of seismic shear waves from earthquakes', *Journal of Geophysical Research* **75**(26), 4997–5009.

Cao, A. and Romanowicz, B. [2004], 'Hemispherical transition of seismic attenuation at the top of the earth's inner core', *Earth and Planetary Science Letters* **228**(3), 243–253.
URL: *https://www.sciencedirect.com/science/article/pii/S0012821X04005862*

Carcolé, E. and Sato, H. [2010], 'Spatial distribution of scattering loss and intrinsic absorption of short-period S waves in the lithosphere of Japan on the basis of the Multiple Lapse Time Window Analysis of Hi-net data', *Geophysical Journal International* **180**(1), 268–290.

Chan, W. W. and Der, Z. A. [1988], 'Attenuation of multiple ScS in various parts of the world', *Geophysical Journal International* **92**(2), 303–314.

Chapman, C., Jen-Yi, C., Lyness, D. and Doornbos, D. [1988], 'The WKBJ seismogram algorithm', *Seismological algorithms: Computational methods and computer programs* pp. 47–74.

Chaves, C. A. and Ritsema, J. [2016], 'The influence of shear-velocity heterogeneity on ScS2/ScS amplitude ratios and estimates of Q in the mantle', *Geophysical Research Letters* **43**(15), 7997–8005.

Cooper, R. F. [2002], 'Seismic wave attenuation: Energy dissipation in viscoelastic crystalline solids', *Reviews in mineralogy and geochemistry* **51**(1), 253–290.

Cormier, V. F. [2020], *Seismic Viscoelastic Attenuation*, Springer International Publishing, Cham, pp. 1–14.
URL: *https://doi.org/10.1007/978-3-030-10475-7*$_5 5 - 1$

Crotwell, H. P., Owens, T. J., Ritsema, J. et al. [1999], 'The TauP Toolkit: Flexible seismic travel-time and ray-path utilities', *Seismological Research Letters* **70**, 154–160.

Cui, C., Lei, W., Liu, Q., Peter, D., Bozdağ, E., Tromp, J., Hill, J., Podhorszki, N. and Pugmire, D. [2024], 'Glad-m35: a joint p and s global tomographic model with uncertainty quantification', *Geophysical Journal International* **239**(1), 478–502.

Dalton, C. A. and Ekström, G. [2006], 'Global models of surface wave attenuation', *Journal of Geophysical Research: Solid Earth* **111**(B5).

Dalton, C. A., Ekström, G. and Dziewoński, A. M. [2008], 'The global attenuation structure of the upper mantle', *Journal of Geophysical Research: Solid Earth* **113**(B9).

Dasios, A., Astin, T. and McCann, C. [2001], 'Compressional-wave Q estimation from full-waveform sonic data', *Geophysical Prospecting* **49**(3), 353–373.

De Wit, R., Käufl, P., Valentine, A. and Trampert, J. [2014], 'Bayesian inversion of free oscillations for Earth's radial (an)elastic structure', *Physics of the Earth and Planetary Interiors* **237**, 1–17.

Der, Z. A. and Lees, A. C. [1985], 'Methodologies for estimating t*(f) from short-period body waves and regional variations of t*(f) in the United States', *Geophysical Journal International* **82**(1), 125–140.

Durand, S., Matas, J., Ford, S., Ricard, Y., Romanowicz, B. and Montagner, J.-P. [2013], 'Insights from scs–s measurements on deep mantle attenuation', *Earth and Planetary Science Letters* **374**, 101–110.

Durek, J. J. and Ekström, G. [1996], 'A radial model of anelasticity consistent with long-period surface-wave attenuation', *Bulletin of the Seismological Society of America* **86**(1A), 144–158.

Dziewonski, A. M. and Anderson, D. L. [1981], 'Preliminary reference Earth model', *Physics of the earth and planetary interiors* **25**(4), 297–356.

Dziewonski, A. M. and Anderson, D. L. [1984], 'Seismic Tomography of the Earth's Interior: The first three-dimenstional models of the earth's structure promise to answer some basic questions of geodynamics and signify a revolution in earth science', *American Scientist* **72**(5), 483–494.

Eberhart-Phillips, D. and Chadwick, M. [2002], 'Three-dimensional attenuation model of the shallow Hikurangi subduction zone in the Raukumara Peninsula, New Zealand', *Journal of Geophys-*

ical Research: Solid Earth **107**(B2), ESE 3–1–ESE 3–15.

URL: *https://agupubs.onlinelibrary.wiley.com/doi/abs/10.1029/2000JB000046*

Eilon, Z. C. and Abers, G. A. [2017], 'High seismic attenuation at a mid-ocean ridge reveals the distribution of deep melt', *Science Advances* **3**(5), e1602829.

URL: *https://www.science.org/doi/abs/10.1126/sciadv.1602829*

Faul, U. H. and Jackson, I. [2015], 'Transient creep and strain energy dissipation: An experimental perspective', **43**, 541–569.

Fehler, M., Hoshiba, M., Sato, H. and Obara, K. [1992], 'Separation of scattering and intrinsic attenuation for the Kanto-Tokai region, Japan, using measurements of S-wave energy versus hypocentral distance', *Geophysical Journal International* **108**(3), 787–800.

Fisher, J. L., Wysession, M. E. and Fischer, K. M. [2003], 'Small-scale lateral variations in d attenuation and velocity structure', *Geophysical research letters* **30**(8).

Flanagan, M. P. and Wiens, D. A. [1994], 'Radial upper mantle attenuation structure of inactive back arc basins from differential shear wave measurements', *Journal of Geophysical Research: Solid Earth* **99**(B8), 15469–15485.

URL: *https://agupubs.onlinelibrary.wiley.com/doi/abs/10.1029/94JB00804*

Ford, S. R., Garnero, E. J. and Thorne, M. S. [2012], 'Differential t* measurements via instantaneous frequency matching: observations of lower mantle shear attenuation heterogeneity beneath western central america', *Geophysical Journal International* **189**(1), 513–523.

Forte, A. M. and Mitrovica, J. X. [2001], 'Deep-mantle high-viscosity flow and thermochemical structure inferred from seismic and geodynamic data', *Nature* **410**(6832), 1049–1056.

French, S. and Romanowicz, B. A. [2014], 'Whole-mantle radially anisotropic shear velocity structure from spectral-element waveform tomography', **199**(3), 1303–1327.

Garcia, R., Schardong, L. and Chevrot, S. [2013], 'A nonlinear method to estimate source parameters, amplitude, and travel times of teleseismic body waves', *Bulletin of the Seismological Society of America* **103**(1), 268–282.

712 Glišović, P., Forte, A. M. and Ammann, M. W. [2015], 'Variations in grain size and viscosity
713 based on vacancy diffusion in minerals, seismic tomography, and geodynamically inferred mantle
714 rheology', *Geophysical Research Letters* **42**(15), 6278–6286.

715 Gomer, B. and Okal, E. [2003], 'Multiple-scs probing of the ontong-java plateau', *Physics of the*
716 *Earth and Planetary Interiors* **138**(3-4), 317–331.

717 Gung, Y. and Romanowicz, B. [2004], 'Q tomography of the upper mantle using three-component
718 long-period waveforms', *Geophysical Journal International* **157**(2), 813–830.

719 Hansen, S. E., Garnero, E. J. and Rost, S. [2021], 'Historical interstation pattern referencing (hipr):
720 An application to pcp waves recorded in the antarctic for ulvz imaging', *Journal of Geophysical*
721 *Research: Solid Earth* **126**(10), e2021JB022741.

722 Hunter, J. D. [2007], 'Matplotlib: A 2D graphics environment', *Computing in Science & Engineering*
723 **9**(3), 90–95.

724 Hwang, Y. K. and Ritsema, J. [2011], 'Radial Qμ structure of the lower mantle from teleseismic
725 body-wave spectra', *Earth and Planetary Science Letters* **303**(3-4), 369–375.

726 Hwang, Y. K., Ritsema, J. and Goes, S. [2009], 'Spatial variations of p wave attenuation in the
727 mantle beneath north america', *Journal of Geophysical Research: Solid Earth* **114**(B6).

728 Höink, T., Lenardic, A. and Richards, M. [2012], 'Depth-dependent viscosity and mantle stress
729 amplification: implications for the role of the asthenosphere in maintaining plate tectonics',
730 *Geophysical Journal International* **191**(1), 30–41.
731 **URL:** *https://doi.org/10.1111/j.1365-246X.2012.05621.x*

732 Isse, T. and Nakanishi, I. [1997], 'The effect of the crust on the estimation of mantle Q from spectral
733 ratios of multiple ScS phases', *Bulletin of the Seismological Society of America* **87**(3), 778–781.

734 Jackson, I. and Faul, U. H. [2010], 'Grainsize-sensitive viscoelastic relaxation in olivine: Towards a
735 robust laboratory-based model for seismological application', *Physics of the Earth and Planetary*
736 *Interiors* **183**(1-2), 151–163.

737 Jackson, I., Fitz Gerald, J. D., Faul, U. H. and Tan, B. H. [2002], 'Grain-size-sensitive seis-
738 mic wave attenuation in polycrystalline olivine', *Journal of Geophysical Research: Solid Earth*
739 **107**(B12), ECV–5.

740 Jackson, I., Paterson, M. and Fitz Gerald, J. [1992], 'Seismic wave dispersion and attenuation in
741 Åheim dunite: an experimental study', *Geophysical Journal International* **108**(2), 517–534.

742 Kanamori, H. and Rivera, L. [2015], 'Near-vertical multiple ScS phases and vertically averaged
743 mantle properties', *Geological Society of America Special Papers* .

744 Kaneshima, S. [2016], 'Seismic scatterers in the mid-lower mantle', *Physics of the Earth and Plan-*
745 *etary Interiors* **257**, 105–114.
746 **URL:** *https://www.sciencedirect.com/science/article/pii/S0031920116300620*

747 Karaoğlu, H. and Romanowicz, B. [2018], 'Inferring global upper-mantle shear attenuation structure
748 by waveform tomography using the spectral element method', *Geophysical Journal International*
749 **213**(3), 1536–1558.

750 Karato, S.-i. [1993], 'Importance of anelasticity in the interpretation of seismic tomography', *Geo-*
751 *physical research letters* **20**(15), 1623–1626.

752 Kido, M. and Čadek, O. [1997], 'Inferences of viscosity from the oceanic geoid: Indication of a
753 low viscosity zone below the 660-km discontinuity', *Earth and Planetary Science Letters* **151**(3-
754 4), 125–137.

755 Konishi, K., Fuji, N. and Deschamps, F. [2017], 'Elastic and anelastic structure of the lowermost
756 mantle beneath the Western Pacific from waveform inversion', *Geophysical Journal International*
757 **208**(3), 1290–1304.

758 Konishi, K., Fuji, N. and Deschamps, F. [2020], 'Three-dimensional elastic and anelastic structure
759 of the lowermost mantle beneath the western Pacific from finite-frequency tomography', *Journal*
760 *of Geophysical Research: Solid Earth* **125**(2), e2019JB018089.

761 Kovach, R. L. and Anderson, D. L. [1964], 'Attenuation of shear waves in the upper and lower
762 mantle', *Bulletin of the Seismological Society of America* **54**(6A), 1855–1864.

763 Lai, H., Garnero, E. J., Grand, S. P., Porritt, R. W. and Becker, T. W. [2019], 'Global travel time
764 data set from adaptive empirical wavelet construction', *Geochemistry, Geophysics, Geosystems*
765 **20**(5), 2175–2198.

766 Lawrence, J. F. and Wysession, M. E. [2006], 'QLM9: A new radial quality factor ($Q\mu$) model for
767 the lower mantle', *Earth and Planetary Science Letters* **241**(3-4), 962–971.

768 Lees, J. M. and Park, J. [1995], 'Multiple-taper spectral analysis: A stand-alone C-subroutine',
769 *Computers & Geosciences* **21**(2), 199–236.

770 Lekić, V., Matas, J., Panning, M. and Romanowicz, B. [2009], 'Measurement and implications of
771 frequency dependence of attenuation', *Earth and Planetary Science Letters* **282**(1-4), 285–293.

772 Liu, C. and Grand, S. P. [2018], 'Seismic attenuation in the African LLSVP estimated from PcS
773 phases', *Earth and Planetary Science Letters* **489**, 8–16.

774 Mao, W. and Zhong, S. [2018], 'Slab stagnation due to a reduced viscosity layer beneath the mantle
775 transition zone', *Nature Geoscience* **11**(11), 876–881.

776 Marquardt, H. and Miyagi, L. [2015], 'Slab stagnation in the shallow lower mantle linked to an
777 increase in mantle viscosity', *Nature Geoscience* **8**(4), 311–314.

778 Matas, J. and Bukowinski, M. S. [2007], 'On the anelastic contribution to the temperature depen-
779 dence of lower mantle seismic velocities', *Earth and Planetary Science Letters* **259**(1), 51–65.
780 **URL:** *https://www.sciencedirect.com/science/article/pii/S0012821X07002555*

781 Matheney, M. P. and Nowack, R. L. [1995], 'Seismic attenuation values obtained from instantaneous-
782 frequency matching and spectral ratios', *Geophysical Journal International* **123**(1), 1–15.

783 McCarthy, C., Takei, Y. and Hiraga, T. [2011], 'Experimental study of attenuation and dispersion
784 over a broad frequency range: 2. The universal scaling of polycrystalline materials', *Journal of*
785 *Geophysical Research: Solid Earth* **116**(B9).

786 Mitrovica, J. and Forte, A. [2004], 'A new inference of mantle viscosity based upon joint inversion
787 of convection and glacial isostatic adjustment data', *Earth and Planetary Science Letters* **225**(1-
788 2), 177–189.

Moulik, P. and Ekström, G. [2025], 'Radial structure of the Earth: (II) Model features and interpretations', *Physics of the Earth and Planetary Interiors* **361**, 107320.
URL: *https://www.sciencedirect.com/science/article/pii/S0031920125000147*

Nguyen, V.-D., Nguyen, L.-M., Nguyen, C.-N., Ha, T.-G., Ha, V.-L., Nguyen, T.-H. and Le, Q.-K. [2025], 'Unveiling the seismic attenuation characteristics in the mantle beneath Southeast Asia: Insights into mantle dynamics and tectonic processes', *Regional Studies in Marine Science* **86**, 104192.
URL: *https://www.sciencedirect.com/science/article/pii/S2352485525001835*

Ogiso, M. [2019], 'A method for mapping intrinsic attenuation factors and scattering coefficients of S waves in 3-D space and its application in southwestern Japan', *Geophysical Journal International* **216**(2), 948–957.

Oki, S. and Shearer, P. M. [2008], 'Mantle Q structure from S-P differential attenuation measurements', *Journal of Geophysical Research: Solid Earth* **113**(B12).

Pang, G., Abers, G. A. and van Keken, P. E. [2023], 'Focusing effects of teleseismic wavefields by the subducting plate beneath Cascadia', *Journal of Geophysical Research: Solid Earth* **128**(6), e2022JB025486.

Pejić, T., Tkalčić, H., Sambridge, M., Cormier, V. F. and Benavente, R. [2017], 'Attenuation tomography of the upper inner core', *Journal of Geophysical Research: Solid Earth* **122**(4), 3008–3032.

Quan, Y. and Harris, J. M. [1997], 'Seismic attenuation tomography using the frequency shift method', *Geophysics* **62**(3), 895–905.

Reid, F., Woodhouse, J. and Van Heijst, H. [2001], 'Upper mantle attenuation and velocity structure from measurements of differential s phases', *Geophysical Journal International* **145**(3), 615–630.

Resovsky, J., Trampert, J. and Van der Hilst, R. [2005], 'Error bars for the global seismic Q profile', *Earth and Planetary Science Letters* **230**(3), 413–423.
URL: *https://www.sciencedirect.com/science/article/pii/S0012821X04007137*

Revenaugh, J. and Jordan, T. H. [1991], 'Mantle Layering From ScS Reverberations: 1. Waveform Inversion From Zeroth-Order Reverberations', *Journal of Geophysical Research: Solid Earth* **96**(B12), 19749–19762.

Ricard, Y., Durand, S., Montagner, J.-P. and Chambat, F. [2014], 'Is there seismic attenuation in the mantle?', *Earth and Planetary Science Letters* **388**, 257–264.

Rietbrock, A. [2001], 'P wave attenuation structure in the fault area of the 1995 Kobe earthquake', *Journal of Geophysical Research: Solid Earth* **106**(B3), 4141–4154.
URL: *https://agupubs.onlinelibrary.wiley.com/doi/abs/10.1029/2000JB900234*

Ritsema, J., Deuss, A., Van Heijst, H. and Woodhouse, J. [2011], 'S40RTS: a degree-40 shear-velocity model for the mantle from new Rayleigh wave dispersion, teleseismic traveltime and normal-mode splitting function measurements', *Geophysical Journal International* **184**(3), 1223–1236.

Romanowicz, B. [1995], 'A global tomographic model of shear attenuation in the upper mantle', *Journal of Geophysical Research: Solid Earth* **100**(B7), 12375–12394.

Romanowicz, B. [1998], 'Attenuation tomography of the earth's mantle: a review of current status', *pure and applied geophysics* **153**, 257–272.

Romanowicz, B. and Gung, Y. [2002], 'Superplumes from the core-mantle boundary to the lithosphere: Implications for heat flux', *Science* **296**(5567), 513–516.

Romanowicz, B. and Mitchell, B. [2015], '1.25—deep earth structure: Q of the earth from crust to core', *Treatise on geophysics* **1**, 789–827.

Rost, S., Earle, P. S., Shearer, P. M., Frost, D. A. and Selby, N. D. [2015], Seismic detections of small-scale heterogeneities in the deep Earth, *in* 'The Earth's heterogeneous mantle: A geophysical, geodynamical, and geochemical perspective', Springer, pp. 367–390.

Rost, S. and Frost, D. A. [2025], 'Global mantle heterogeneity structure from scattered PKPPKP', *Earth and Planetary Science Letters* **664**, 119415.
URL: *https://www.sciencedirect.com/science/article/pii/S0012821X25002146*

841 Roth, E. G., Wiens, D. A., Dorman, L. M., Hildebrand, J. and Webb, S. C. [1999], 'Seismic atten-
842 uation tomography of the Tonga-Fiji region using phase pair methods', *Journal of Geophysical*
843 *Research: Solid Earth* **104**(B3), 4795–4809.
844 **URL:** *https://agupubs.onlinelibrary.wiley.com/doi/abs/10.1029/1998JB900052*

845 Rudolph, M. L., Lekić, V. and Lithgow-Bertelloni, C. [2015], 'Viscosity jump in Earth's mid-
846 mantle', *Science* **350**(6266), 1349–1352.
847 **URL:** *https://www.science.org/doi/abs/10.1126/science.aad1929*

848 Scherbaum, F. [1990], 'Combined inversion for the three-dimensional Q structure and source
849 parameters using microearthquake spectra', *Journal of Geophysical Research: Solid Earth*
850 **95**(B8), 12423–12438.
851 **URL:** *https://agupubs.onlinelibrary.wiley.com/doi/abs/10.1029/JB095iB08p12423*

852 Shearer, P. [2007], 1.20 - Deep Earth Structure – Seismic Scattering in the Deep Earth, *in* G. Schu-
853 bert, ed., 'Treatise on Geophysics', Elsevier, Amsterdam, pp. 695–729.
854 **URL:** *https://www.sciencedirect.com/science/article/pii/B9780444527486000213*

855 Sheehan, A. F. and Solomon, S. C. [1992], 'Differential shear wave attenuation and its lateral varia-
856 tion in the North Atlantic region', *Journal of Geophysical Research: Solid Earth* **97**(B11), 15339–
857 15350.

858 Soto Castaneda, R. A., Abers, G. A., Eilon, Z. C. and Christensen, D. H. [2021], 'Teleseismic At-
859 tenuation, Temperature, and Melt of the Upper Mantle in the Alaska Subduction Zone', *Journal*
860 *of Geophysical Research: Solid Earth* **126**(7), e2021JB021653.
861 **URL:** *https://agupubs.onlinelibrary.wiley.com/doi/abs/10.1029/2021JB021653*

862 Souriau, A., Rivera, L., Maggi, A. and Lévêque, J.-J. [2012], 'Seismic attenuation in the eastern
863 Australian and Antarctic plates, from multiple ScS waves', *Geophysical Journal International*
864 **190**(1), 569–579.
865 **URL:** *https://doi.org/10.1111/j.1365-246X.2012.05501.x*

866 Suetsugu, D., Shiobara, H., Sugioka, H., Ito, A., Isse, T., Ishihara, Y., Tanaka, S., Obayashi, M.,

Tonegawa, T., Yoshimitsu, J. et al. [2019], 'High Q ScS beneath the Ontong Java Plateau', *Earth, Planets and Space* **71**, 1–9.

Sun, S., Ricard, Y., Durand, S. and Debayle, E. [2025], 'A high attenuation layer around 1000 km depth', *Earth and Planetary Science Letters* **669**, 119577.

Talavera-Soza, S., Cobden, L., Faul, U. H. and Deuss, A. [2025], 'Global 3D model of mantle attenuation using seismic normal modes', *Nature* **637**(8048), 1131–1135.

Teng, T.-L. [1968], 'Attenuation of body waves and the Q structure of the mantle', *Journal of Geophysical Research* **73**(6), 2195–2208.

Thomson, D. [1982], 'Spectrum estimation and harmonic analysis', *Proceedings of the IEEE* **70**(9), 1055–1096.

Thrastarson, S., van Herwaarden, D.-P., Noe, S., Josef Schiller, C. and Fichtner, A. [2024], 'RE-VEAL: A global full-waveform inversion model', **114**(3), 1392–1406.

Wang, X., Li, Q., Li, G., Zhou, Y., Ye, Z. and Zhang, H. [2018], 'Seismic triplication used to reveal slab subduction that had disappeared in the late Mesozoic beneath the northeastern South China Sea', *Tectonophysics* **727**, 28–40.

Warren, L. M. and Shearer, P. M. [2002], 'Mapping lateral variations in upper mantle attenuation by stacking P and PP spectra', *Journal of Geophysical Research: Solid Earth* **107**(B12), ESE 6–1–ESE 6–11.
URL: *https://agupubs.onlinelibrary.wiley.com/doi/abs/10.1029/2001JB001195*

Warren, L. M. and Shearer, P. M. [2006], 'Systematic determination of earthquake rupture directivity and fault planes from analysis of long-period P-wave spectra', *Geophysical Journal International* **164**(1), 46–62.

Waszek, L. and Deuss, A. [2013], 'A low attenuation layer in the Earth's uppermost inner core', *Geophysical Journal International* **195**(3), 2005–2015.
URL: *https://doi.org/10.1093/gji/ggt368*

Waszek, L., Schmerr, N. C. and Ballmer, M. D. [2018], 'Global observations of reflectors in the mid-mantle with implications for mantle structure and dynamics', *Nature communications* **9**(1), 385.

Weber, Z. [2000], 'Seismic traveltime tomography: a simulated annealing approach', *Physics of the Earth and Planetary Interiors* **119**(1-2), 149–159.

Widmer, R., Masters, G. and Gilbert, F. [1991], 'Spherically symmetric attenuation within the Earth from normal mode data', *Geophysical journal international* **104**(3), 541–553.

Zaroli, C., Debayle, E. and Sambridge, M. [2010], 'Frequency-dependent effects on global S-wave traveltimes: wavefront-healing, scattering and attenuation', *Geophysical Journal International* **182**(2), 1025–1042.

Zhang, B., Ni, S. and Chen, Y. [2019], 'Seismic attenuation in the lower mantle beneath Northeast China constrained from short-period reflected core phases at short epicentral distances', *Earth and Planetary Physics* **3**(6), 537–546.

Zhao, C., Garnero, E. J., McNamara, A. K., Schmerr, N. and Carlson, R. W. [2015], 'Seismic evidence for a chemically distinct thermochemical reservoir in Earth's deep mantle beneath Hawaii', *Earth and Planetary Science Letters* **426**, 143–153.

Zhu, M., Sun, S., Zhou, Y. and Wu, Q. [2022], 'Mantle q structure from s, ss, sss and ssss amplitude measurements', *Geophysical Journal International* **231**(1), 703–716.

Supplementary materials for

Q_{M1D}: A 1D model of shear attenuation in the mantle from differential body waves

Carl Martin[1,2*], Sujania Talavera-Soza[1] & Arwen Deuss[1]

[1] Department of Geosciences, Utrecht University, 3584 CB, Netherlands

[2] Research School of Earth Sciences, The Australian National University, Canberra, ACT 0200, Australia

*Corresponding author (carl.martin@anu.edu.au)

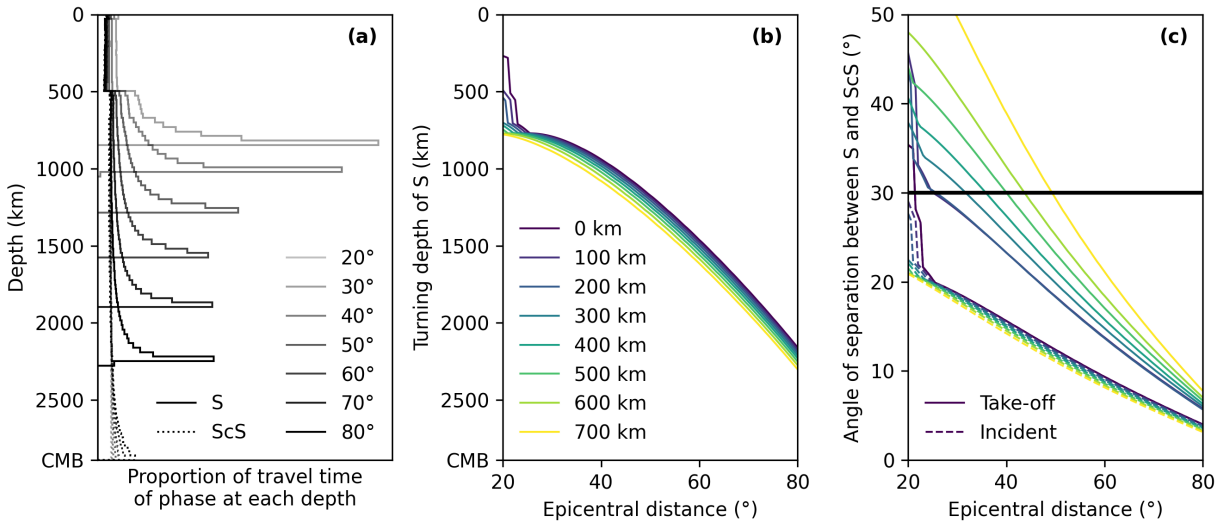

Figure S1: **(a)** The proportion of travel time of each of S and ScS body waves spent at each depth as a function of epicentral distance. **(b)** The turning depth of S waves as a function of epicentral distance. **(c)** The difference between S and ScS angles at take-off (from the event) and incident (at the receiver).

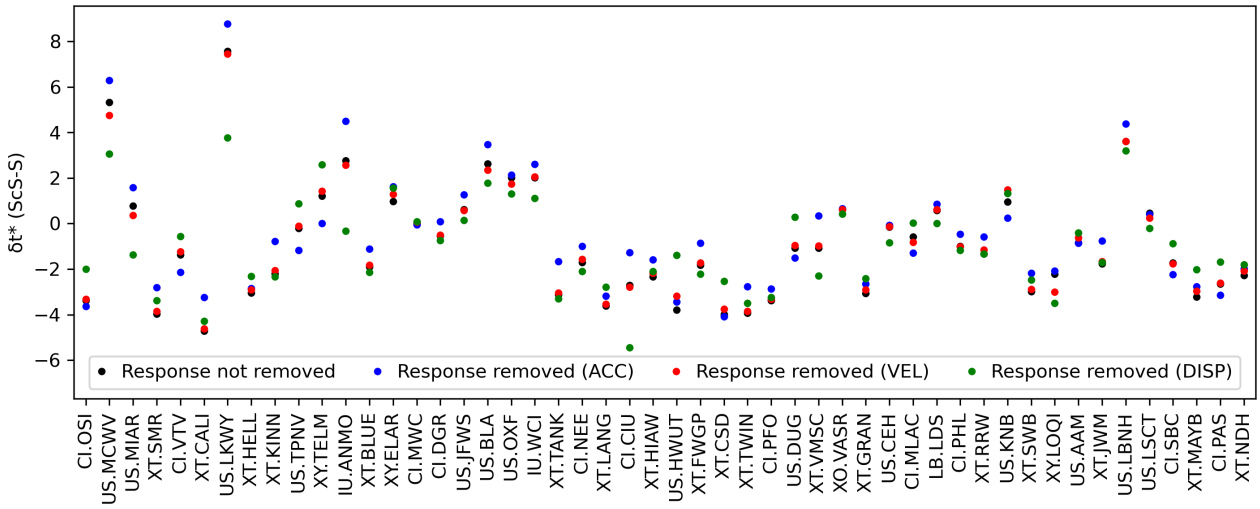

Figure S2: $\delta t^*_{\mathrm{ScS-S}}$ measurements for a selection of 50 stations for the event on 1997/11/28, as used by Ford et al. [2012], for data which has been downloaded. Values are for data with station response not removed (black) and removed and processed as acceleration (blue), velocity (red), and displacement (green).

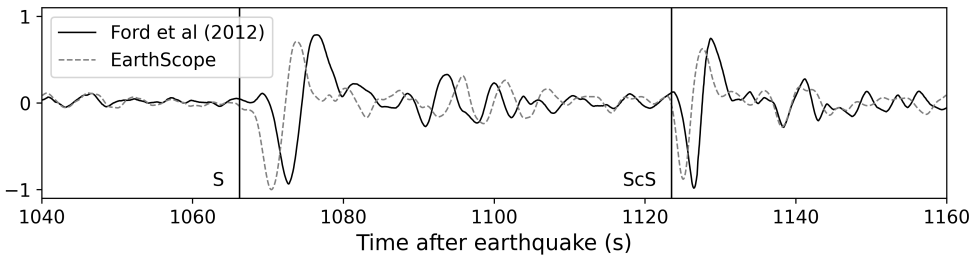

Figure S3: Normalised tangential component of broadband velocity for data downloaded through IRIS Client (EarthScope Consortium) and data reproduced from Figure 1 from Ford et al. [2012], extracted using WebPlotDigitizer. Arrival times computed for S and ScS phases in PREM are overlaid. Data is from station CI.PLM for the Mw 6.6 event on 1997/11/28.

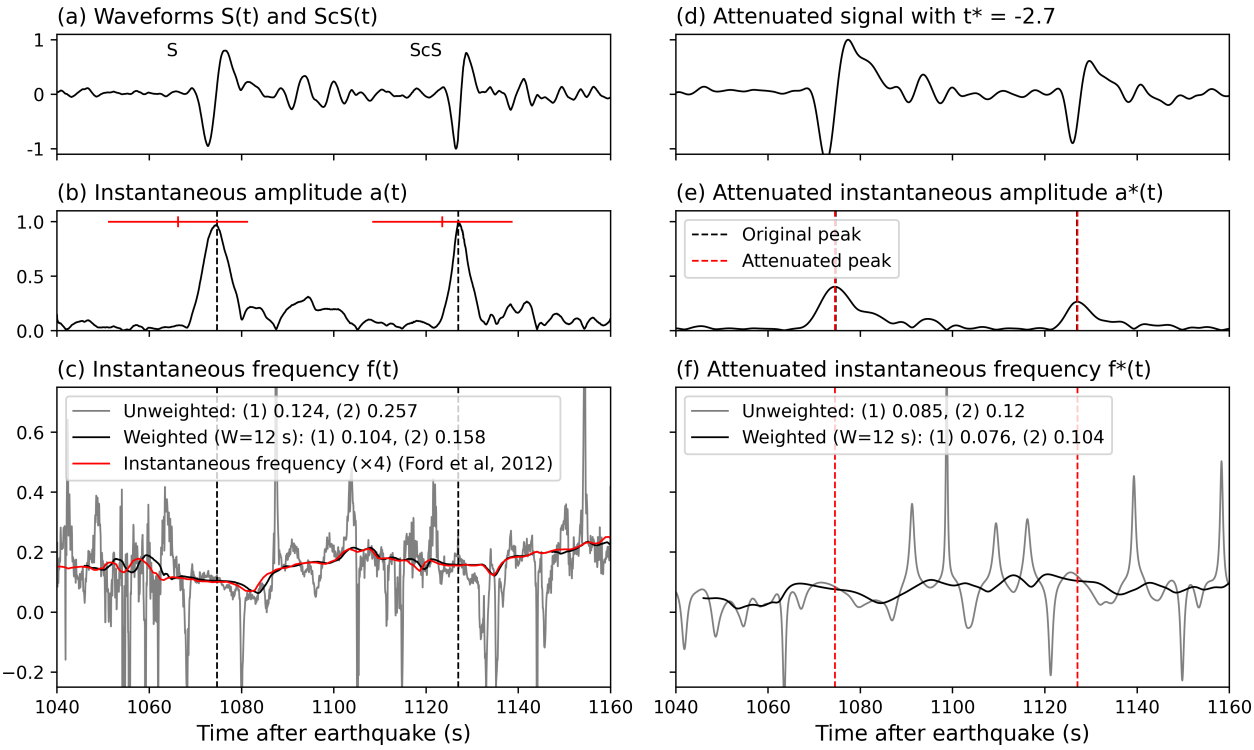

Figure S4: **(a)** Normalised tangential component of broadband velocity reproduced from Figure 1 from Ford et al. [2012], extracted using WebPlotDigitizer. **(b)** Instantaneous amplitude of data, with the peak amplitude highlighted within a search window from the predicted PREM arrival times computed for S and ScS phases. **(c)** The instantaneous frequency computed using Equations 5 (unweighted) and 7 (weighted). The values obtained by Ford et al. [2012] are overlaid in red. **(d)** The attenuated waveforms computed from convolving the waveform with the attenuation operator, Equation 3, for the optimal t^* operator value. **(e)** The instantaneous amplitude of the attenuated waveform, with the original and shifted peaks of the attenuated waveform highlighted. **(f)** The unweighted and weighted instantaneous frequency of the attenuated waveform, showing that the attenuated instantaneous frequency for ScS now matches the original instantaneous frequency for S.

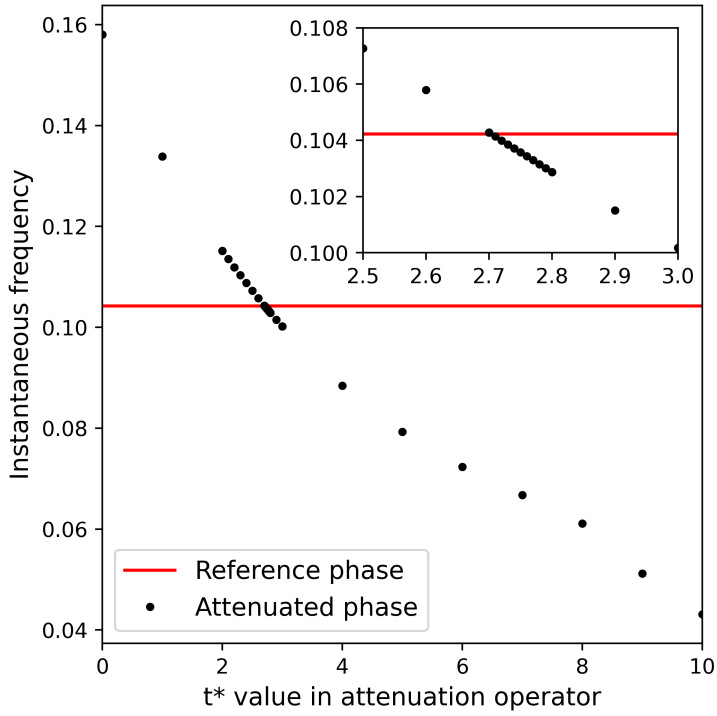

Figure S5: The attenuation factor t^* is obtained by iteratively searching within increments of 1, 0.1 and 0.01 such that the instantaneous frequency of the target phase most closely matches that of the reference phase.

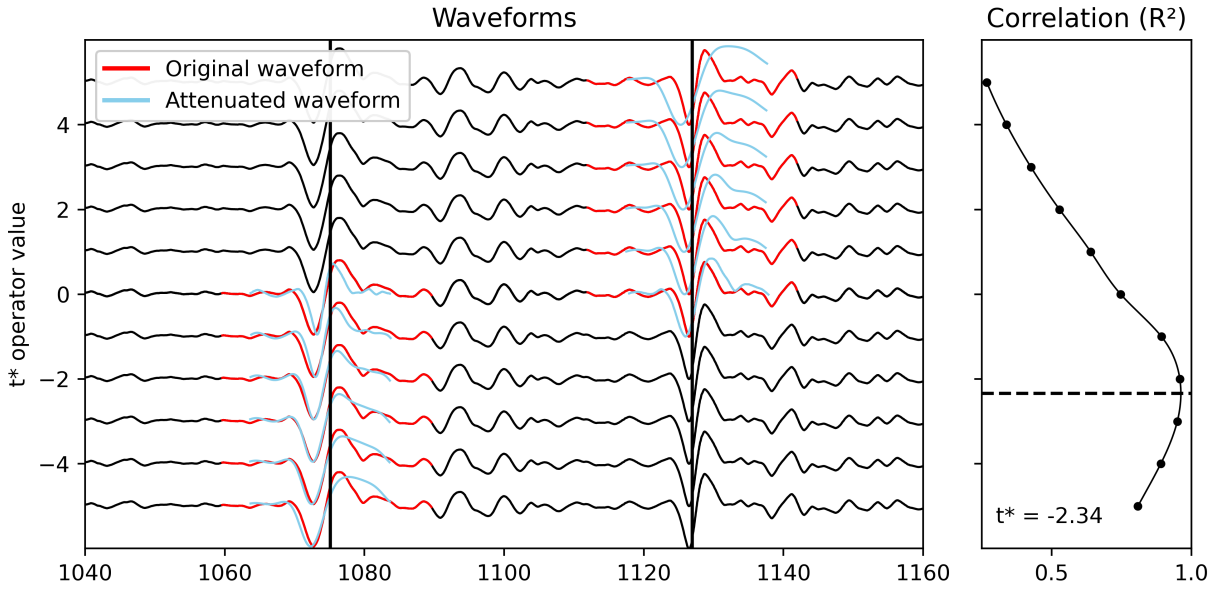

Figure S6: Same as Figure 3f-g but for data from Figure S3. $\delta t^*_{\mathrm{IFM}}$ is -2.70 s and δt^*_{WM} is -2.34 s.

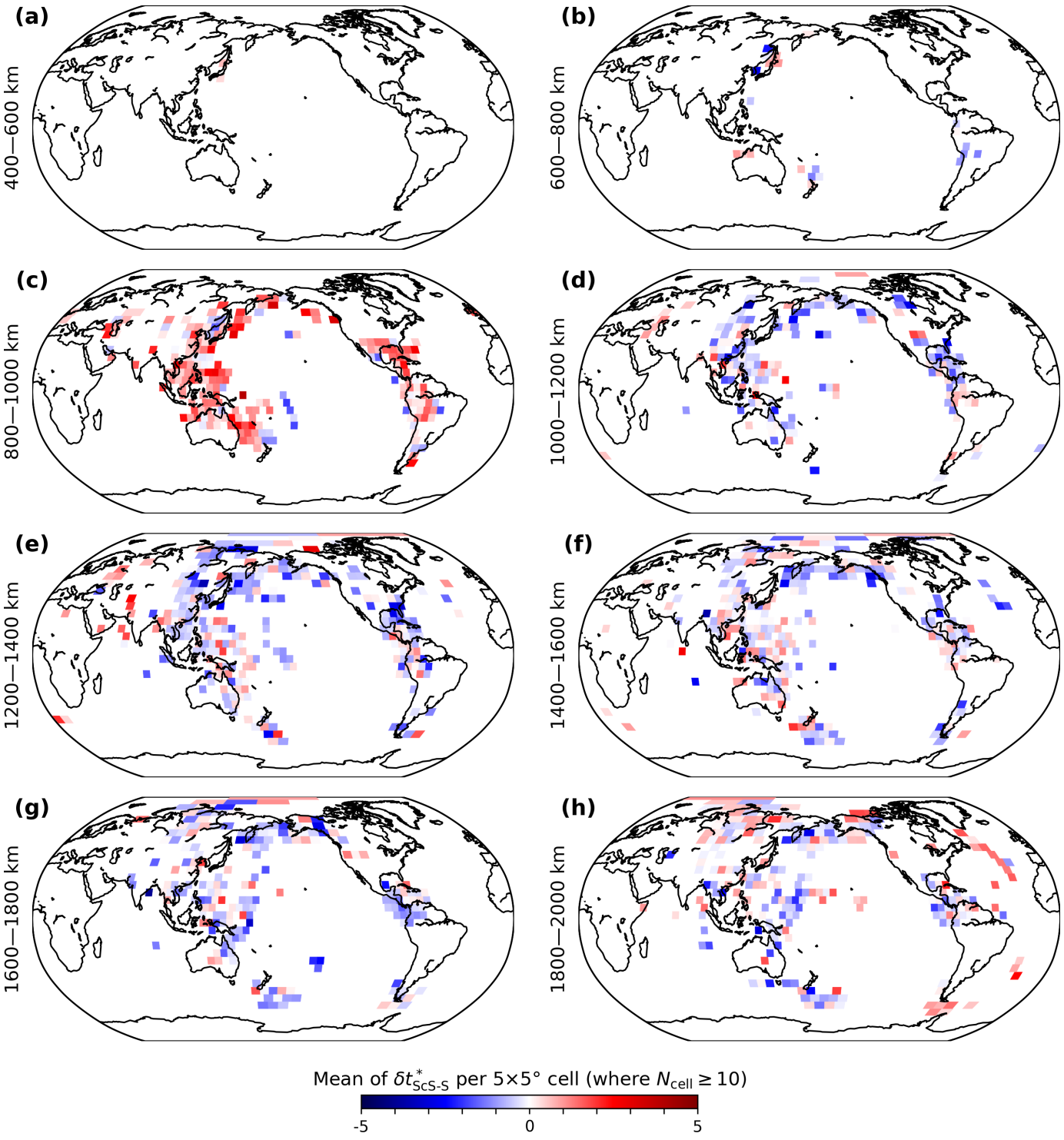

Figure S7: Mean value of $\delta t^*_{\mathrm{ScS\text{-}S}}$ per $5 \times 5°$ cell where grid cells with fewer than 10 ScS bounce points have been omitted, binned according to the turning depth of the S raypath: **(a)** 400–600, **(b)** 600–800, **(c)** 800–1000, **(d)** 1000–1200, **(e)** 1200–1400, **(f)** 1400–1600, **(g)** 1600–1800 and **(h)** 1800–2000 km.

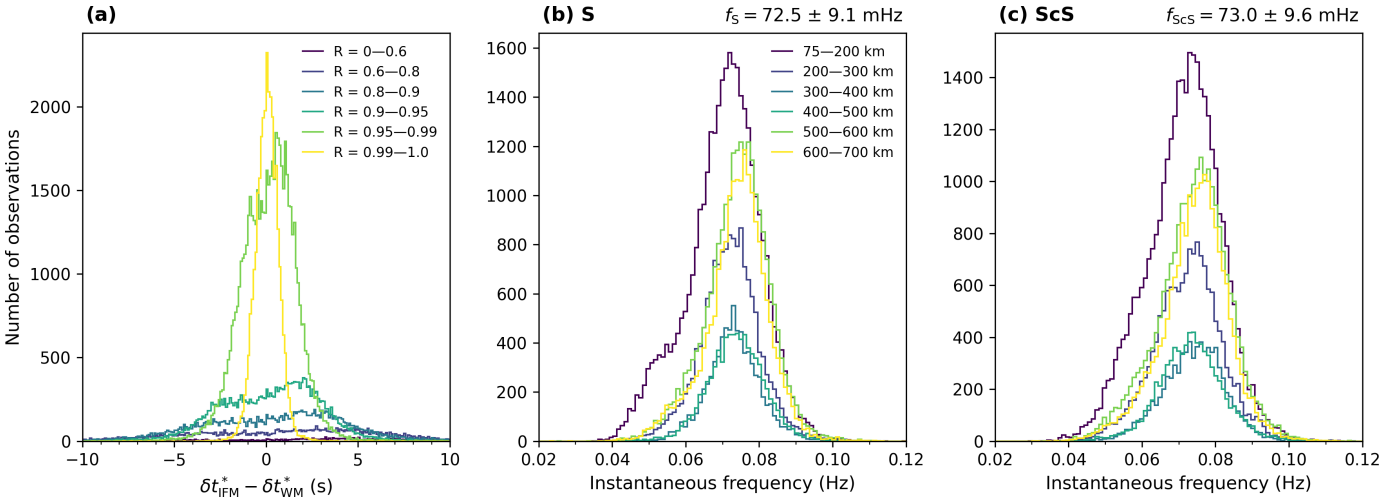

Figure S8: Histogram distribution of instantaneous frequency measurements of **(a)** S and **(b)** ScS, binned by event depth. S is on average more attenuated than ScS.

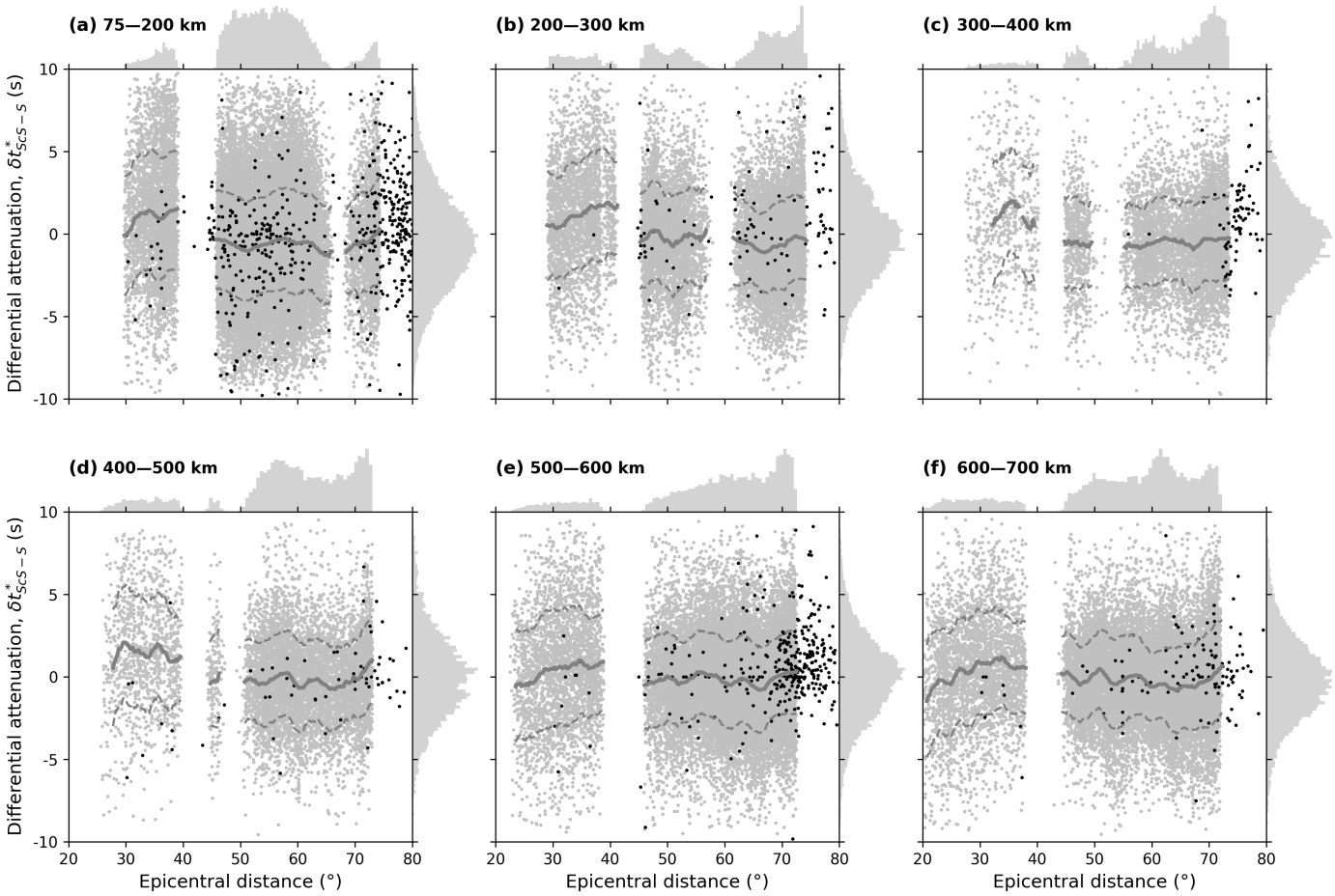

Figure S9: The dataset of differential attenuation $\delta t^*_{\text{ScS-S}}$ measurements reproduced from Figure 4 (grey), with constructed measurements of differential attenuation $t^*_{\text{ScS}} - t^*_{\text{S}}$ from the published dataset of Lai et al. [2019] (black). Aggregated trends of these measurements for events deeper and shallower than 200 km are plotted in Figure 5.

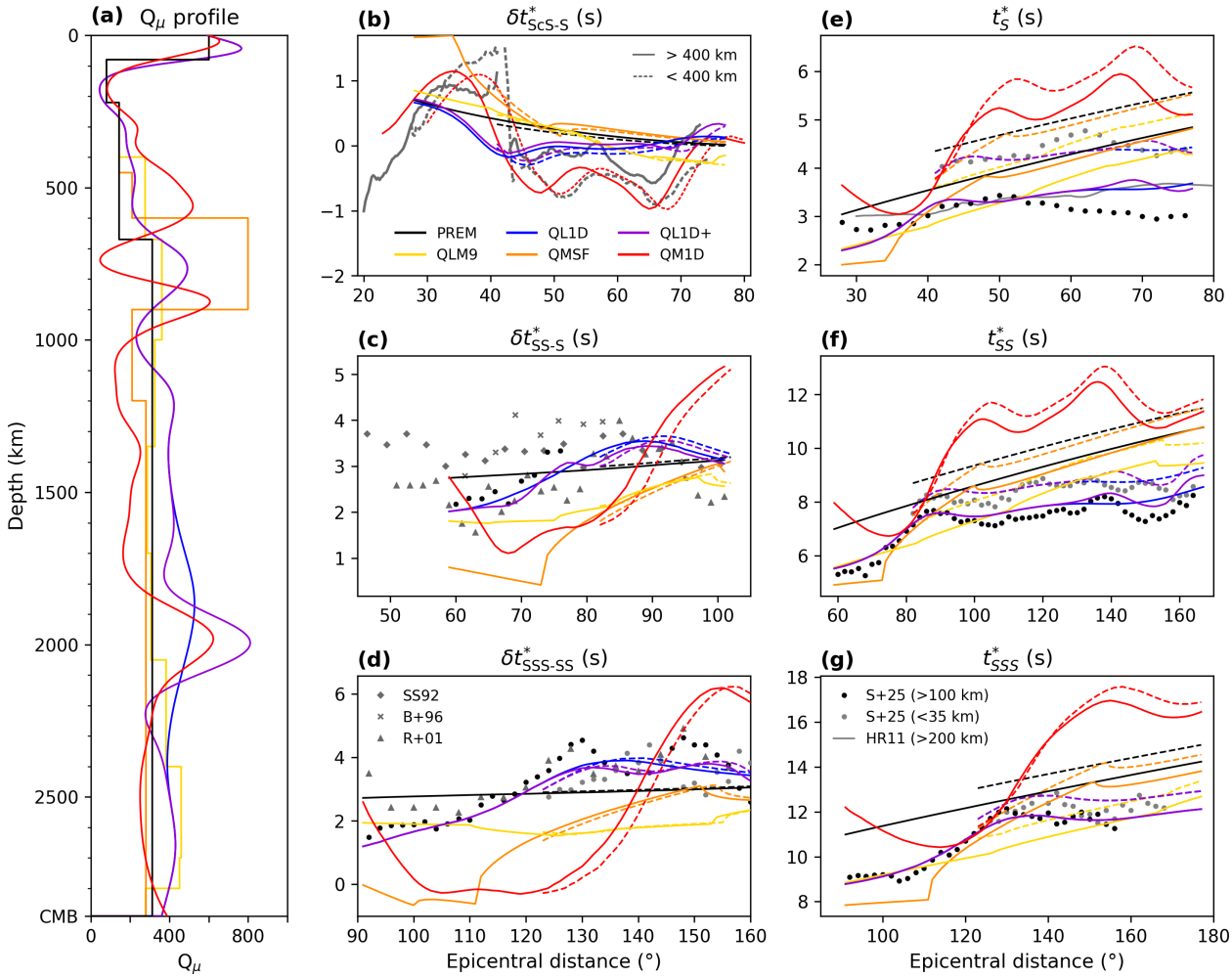

Figure S10: **(a)** Q_μ profiles of PREM (black), QLM9 (yellow), QMSF (orange), QM1D (red), QL1D (blue) and a modified version of QLID with a Ricker wavelet superimposed at a depth of 2000 km (purple). **(b)** Predictions of relative attenuation $\delta t^*_{\text{ScS-S}}$ for each of the models overlaid on data from this study, using a 5° rolling window, for deeper (> 400 km, solid) and shallower (> 400 km, dashed) events. Predictions of differential attenuation **(c)** $\delta t^*_{\text{SS-S}}$ and **(d)** $\delta t^*_{\text{SSS-SS}}$ and absolute attenuation **(e)** t^*_{S}, **(f)** t^*_{SS} and **(g)** t^*_{SSS} for each of the Q_μ profiles. The mean measurements of $\delta t^*_{\text{SS-S}}$, $\delta t^*_{\text{SSS-SS}}$, t^*_{S}, t^*_{SS} and t^*_{SSS} for deep (black dots) and shallow (grey dots) events were constructed from the Sun et al. [2025] dataset. Datasets from other studies are also included for reference where aggregated data was available: t^*_{S} by Hwang and Ritsema [2011] (grey line, note that data has been fixed to match PREM at 30°); $\delta t^*_{\text{SS-S}}$ by Sheehan and Solomon [1992] (grey crosses) and Bhattacharyya et al. [1996] (grey diamonds); and $\delta t^*_{\text{SS-S}}$ and $\delta t^*_{\text{SSS-SS}}$ by Reid et al. [2001] (grey triangles).

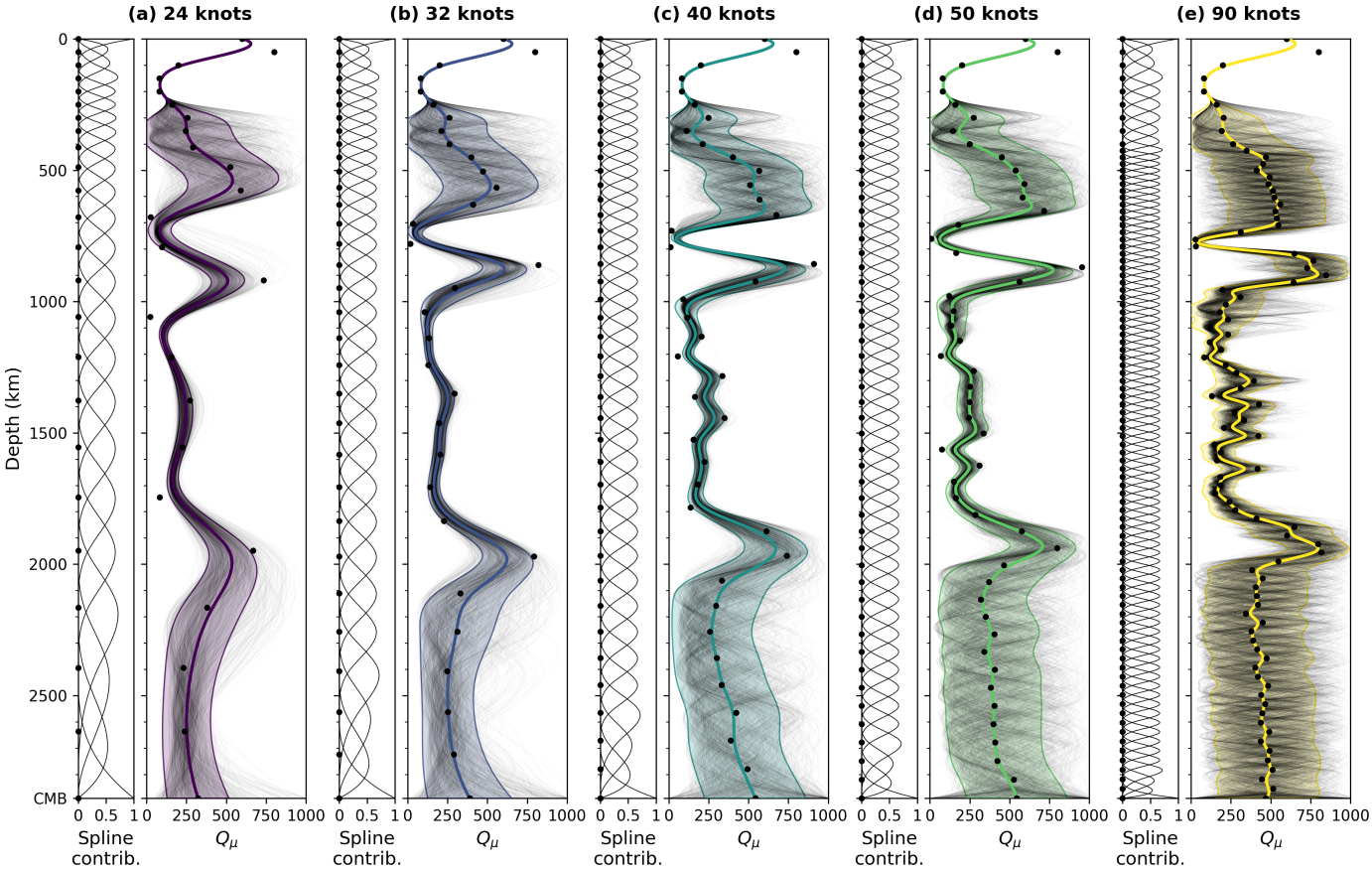

Figure S11: Cubic B-spline basis functions and inversion results for **(a)** 24, **(b)** 32, **(c)** 40, **(d)** 50 and **(e)** 90 depth knots.

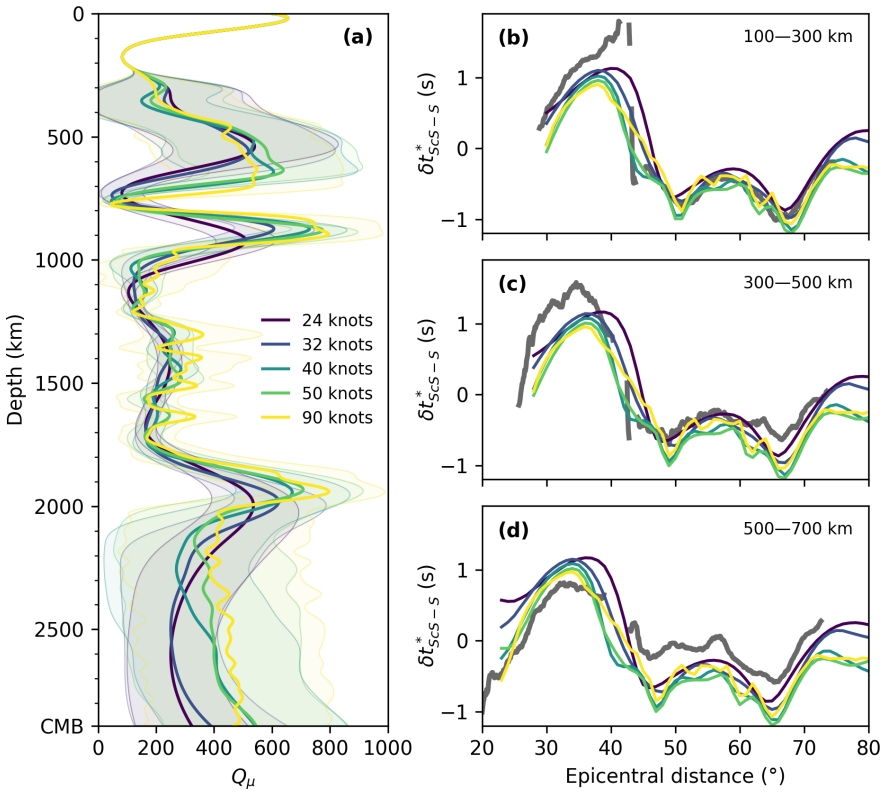

Figure S12: **(a)** Comparison of mean inversion Q_μ profiles for the different numbers of depth knots in Figure S11. Predictions of $\delta t^*_{\text{ScS-S}}$ for each of the models overlaid on data from this study for event depths **(b)** 100–300, **(c)** 300–500 and **(d)** 500–700 km, using a 5° rolling window.

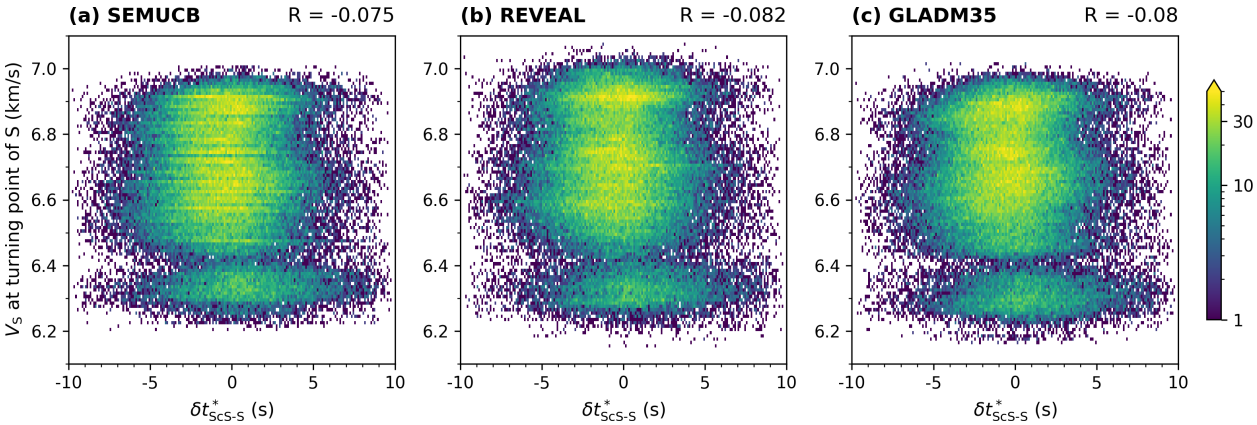

Figure S13: Plots of our measured values of $\delta t^*_{\text{ScS-S}}$ compared to the velocity at the turning depth of the S raypaths for three full waveform tomographic models of the mantle: **(a)** SEMUCB-WM1 [French and Romanowicz, 2014], **(b)** REVEAL [Thrastarson et al., 2024] and **(c)** GLAD-M35 [Cui et al., 2024]. The Pearson correlation coefficient R is computed for each comparison.

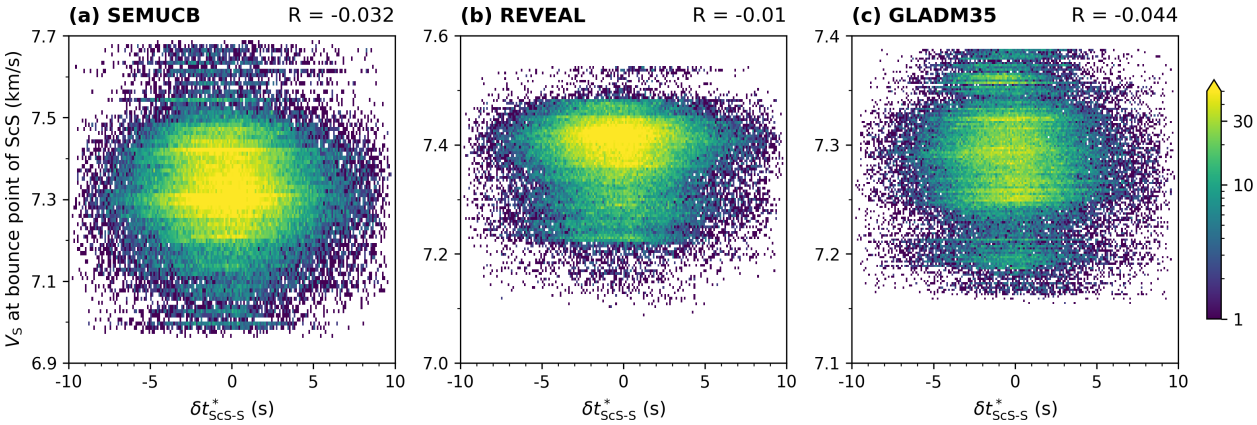

Figure S14: Plots of our measured values of $\delta t^*_{\mathrm{ScS\text{-}S}}$ compared to the velocity at the bounce point of the ScS raypaths for three full waveform tomographic models of the mantle: **(a)** SEMUCB-WM1 [French and Romanowicz, 2014], **(b)** REVEAL [Thrastarson et al., 2024] and **(c)** GLAD-M35 [Cui et al., 2024]. The Pearson correlation coefficient R is computed for each comparison.

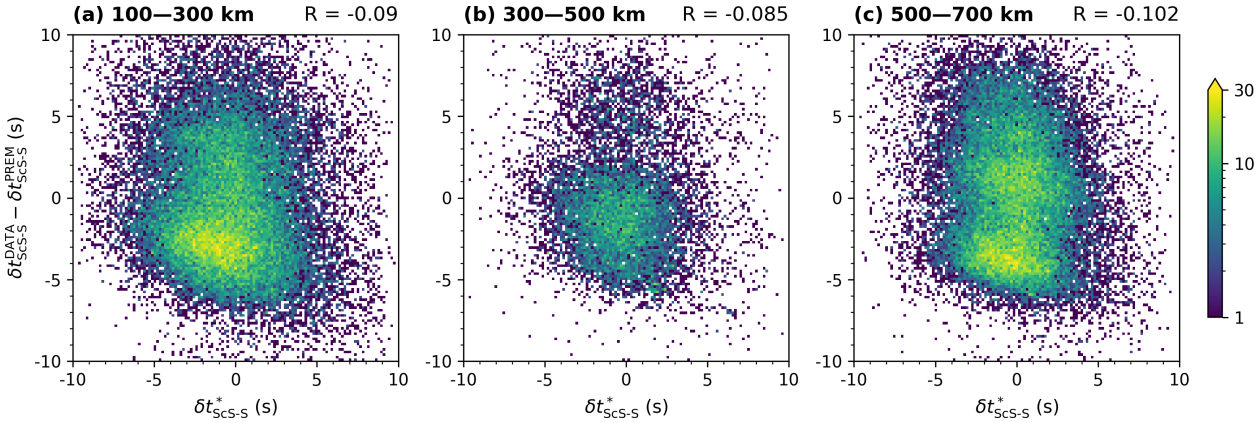

Figure S15: Plots of our measured values of $\delta t^*_{\mathrm{ScS\text{-}S}}$ compared to the difference between the observed travel time differences (corrected for attenuation) and predicted travel time differences for PREM $\delta t^{\mathrm{DATA}}_{\mathrm{ScS\text{-}S}} - \delta t^{\mathrm{PREM}}_{\mathrm{ScS\text{-}S}}$, for the same event depth ranges as Figure 7: **(a)** 100–300, **(b)** 300–500 and **(c)** 500–700 km. The Pearson correlation coefficient R is computed for each comparison.

References

Bhattacharyya, J., Masters, G. and Shearer, P. [1996], 'Global lateral variations of shear wave attenuation in the upper mantle', *Journal of Geophysical Research: Solid Earth* **101**(B10), 22273–22289.

Cui, C., Lei, W., Liu, Q., Peter, D., Bozdağ, E., Tromp, J., Hill, J., Podhorszki, N. and Pugmire, D. [2024], 'Glad-m35: a joint p and s global tomographic model with uncertainty quantification', *Geophysical Journal International* **239**(1), 478–502.

Ford, S. R., Garnero, E. J. and Thorne, M. S. [2012], 'Differential t* measurements via instantaneous frequency matching: observations of lower mantle shear attenuation heterogeneity beneath western central america', *Geophysical Journal International* **189**(1), 513–523.

French, S. and Romanowicz, B. A. [2014], 'Whole-mantle radially anisotropic shear velocity structure from spectral-element waveform tomography', **199**(3), 1303–1327.

Hwang, Y. K. and Ritsema, J. [2011], 'Radial Qμ structure of the lower mantle from teleseismic body-wave spectra', *Earth and Planetary Science Letters* **303**(3-4), 369–375.

Lai, H., Garnero, E. J., Grand, S. P., Porritt, R. W. and Becker, T. W. [2019], 'Global travel time data set from adaptive empirical wavelet construction', *Geochemistry, Geophysics, Geosystems* **20**(5), 2175–2198.

Reid, F., Woodhouse, J. and Van Heijst, H. [2001], 'Upper mantle attenuation and velocity structure from measurements of differential s phases', *Geophysical Journal International* **145**(3), 615–630.

Sheehan, A. F. and Solomon, S. C. [1992], 'Differential shear wave attenuation and its lateral variation in the North Atlantic region', *Journal of Geophysical Research: Solid Earth* **97**(B11), 15339–15350.

Sun, S., Ricard, Y., Durand, S. and Debayle, E. [2025], 'A high attenuation layer around 1000 km depth', *Earth and Planetary Science Letters* **669**, 119577.

Thrastarson, S., van Herwaarden, D.-P., Noe, S., Josef Schiller, C. and Fichtner, A. [2024], 'REVEAL: A global full-waveform inversion model', **114**(3), 1392–1406.